Measurement of Electron–Helicity Dependent Cross Sections of Deeply Virtual Compton Scattering with CEBAF at 11 GeV

Mongi Dlamini

February 19, 2015

Advisory and Examination Committee

Prof. Julie Roche

_____

Thesis Advisor

Prof. Charlotte Elster

_____

Committee Member

Prof. Carl R. Brune

_____

Committee Member

Prof. Jennifer V. Hines

_____

Committee Member

Abstract

The third Deeply Virtual Compton Scattering experiment (E12-06-114) will run at the Thomas Jefferson National Accelerator Facility's (TJNAF) Hall A beginning in the fall of 2014 to the summer of 2015. The experiment will measure both helicity-dependent and helicity-independent cross sections of the H$(e, e'\gamma)p$ DVCS process in a wide Q^2 range (from 3 to 9 GeV^2), made possible by the recent 12 GeV upgrade, at different values of Bjorken-x(x_B from 0.36 to 0.60). A measurement over this range in Q^2 will provide a strong test of the Generalized Parton Distribution(GPD) formalism in parametrizing the interior structure of the proton. This proposal presents my involvement in the DVCS collaboration and experiment up to this point. I also provide a time-line and a plan for future projects, leading to a Spring 2017 graduation.

Contents

I Introduction

Electrons, protons and neutrons are the building blocks of the visible matter of the universe. The electron was discovered in 1897 by J.J. Thompson, the proton in 1919 by E. Rutherford and the neutron in 1932 by J. Chadwick. Electrons are structure-less and their interaction with matter is described by a mathematical framework known as Quantum Electrodynamics (QED). Protons and neutrons are building blocks of the nucleus and are collectively called nucleons. Until 1933, nucleons were thought to be structure-less like electrons. This picture changed when O. Stern (1933) measured the magnetic moment of the proton and found it to be approximately twice as large as predicted for elementary particles of spin $\frac{1}{2}$ and mass m.

Experimental and theoretical efforts have led to the description of nucleons as extended bodies composed of quarks and gluons, and as part of a class of particles called hadrons. The mathematical framework which describes the dynamics of hadrons from the interactions of quarks and gluons is called Quantum Chromodynamics (QCD). The QCD force is responsible for keeping nucleons and nuclei as a unit and is called the strong force. There are many mysteries about this force. As an example, the role of gluons, the sea of quarks, their interactions and contribution to nucleon and nuclei properties is still not well understood. Another interesting aspect of QCD is that unlike the other forces of nature (weak, electromagnetic, and gravitational), the strong force does not obey the inverse square law. This is a result of the nature of the strong coupling "constant",α_s, which is a running parameter as a function of the energy scale. This principle leads to two important consequences:

1. Asymptotic freedom: at very short distances (high energies), the force is the weakest, meaning the coupling constant becomes small, reducing the interaction between the quarks and the gluons. In this configuration, the nucleon can be said to be "frozen" with respect to a relativistic lepton probe and this allows a perturbative treatment of QCD and an experimental access window where QCD calculations have been tested [1].

2. Confinement: at large distances (comparable to hadron size), the force increases [2]. As a result, there are no free quarks. Understanding QCD in the confinement regime is a challenge that has become an important occupation in nuclear physics. In as much as QCD explains how the constituents of nucleons interact, there is still a number of outstanding questions related to the nucleon system:

- QCD cannot analytically explain confinement.

- What does the interior of a nucleon look like in terms of quark-gluon distribution?

- How much of the nucleon spin is carried by the quarks and how much by the gluons?

In the absence of analytical answers to these and many other questions, experimental advances and nucleon structure models play a significant role in investigating nucleon systems [3].

Many frameworks have been formulated to investigate the structure of nucleons based on their ultimate constituents. The parton model describes the nucleon as an extended body made of 3 valence quarks and a sea of fluctuating quarks and gluons. These nucleon constituents are called partons and each parton is understood to possess a fraction of the nucleon's momentum and to contribute to a fraction of the nucleon's spin. Generalized Parton Distributions(GPDs) build on the parton model to introduce functions that parametrize nucleon structure by presenting the correlation between position and momentum of quarks and gluons. The GPD framework gives a 3-dimensional picture of the

partonic structure of the nucleon. A clean way to measure GPDs is the Deeply Virtual Compton Scattering (DVCS) process.

Pioneer DVCS experiments took place about 2 decades ago and confirmed the feasibility of measuring the DVCS process. These are the H1 and ZEUS collaborations at HERA, the HERMES collaboration at DESY and the CLAS collaboration at the Thomas Jefferson National Accelerator Facility (TJNAF). These experiments resulted in low statistics since they were run in already experimental facilities, not dedicated DVCS setups [1]. Later on, dedicated experiments were planned to run at the TJNAF (Halls A and B) at 6 GeV beam energy, and HERMES. With the recent 12 GeV upgrade, TJNAF offers high precision DVCS measurements and an expanded kinematic region to test the GPD formalism. Experiment E12-06-114 is the first DVCS experiment to run at the TJNAF after the 12 GeV upgrade and is the subject of the proposed thesis work presented by this document.

This document is organized as follows:

- In section II, a brief introduction of the theoretical background in the study of the nucleon structure in the Generalized Parton Distribution framework is presented. In the same section, the experimental context of nucleon structure study, with particular emphasis on DVCS, is also presented. A brief overview of GPD models and fitting techniques is also presented.

- Section III presents an overview of the upcoming experiment(Experiment E12-06-114). This includes an overview of the standard Hall A equipment at the TJNAF and the additional DVCS electromagnetic calorimeter.

- Sections IV and V present my contribution to the DVCS collaboration up to this point and a proposed time-line for my thesis, respectively.

II Formalism

II.I Generalized Parton Distributions(GPDs)

When using an electromagnetic (a lepton) probe to study a nucleon system, two distinct regimes characterize the interaction, a perturbative and a non-perturbative part. In the non-perturbative regime, the strong interaction can be factorized into structure functions. In this approach, one distinguishes a regime where the lepton and the nucleon see each other as point-like structures, characterized by short distances and a hard sub-process from a complex, long distance, soft structure of the nucleon [7], where the lepton probe sees the nucleon as a composite system. Understanding the soft part calls for solving the QCD Lagrangian in its non-perturbative regime, a challenge in nuclear physics at present. Using electromagnetic probes, this soft structure can be accessed via two complimentary processes. One is Deep Inelastic Scattering (DIS) which factorizes the soft structure into Parton Distribution Functions(PDFs) representing the longitudinal momentum and spin distribution of partons in a fast moving nucleon. In this formalism, the assumption is that the transverse momentum of the partons in the fast moving nucleon is negligibly small. Two structure functions parametrize the cross section in this regime [5]:

$$
\begin{aligned}
W_1(\nu, Q^2) &= \sum_q e_q^2 \frac{q(x)}{2M} \quad \equiv \frac{1}{M} F_1(x) \\
W_2(\nu, Q^2) &= \sum_q e_q^2 x q(x) \quad \equiv F_2(x),
\end{aligned}
\tag{1}
$$

with the unpolarized cross section given by [1]:

$$\frac{d^2\sigma}{d\Omega d\nu} = \frac{\alpha^2}{4E^2 sin^4(\frac{\theta_e}{2})} \frac{E'}{E} \left\{ W_2 cos^2(\frac{\theta_e}{2}) + 2W_1 sin^2(\frac{\theta_e}{2}) \right\} \qquad (2)$$

In the limit $(Q^2, \nu) \to \infty$, the Bjorken regime, these structure functions cease to vary with Q^2, a property called scaling. In the Bjorken picture, scaling means quarks become point-like objects at very short distances. The scaling property is, however, violated in QCD by gluon radiation at low parton momentum fraction x, as Q^2 increases [5].

On the other hand, elastic scattering factorizes the soft structure into Form Factors, representing, via a Fourier transform, the spatial distribution of electromagnetic currents in the nucleon, in the plane transverse to the nucleon's direction [7]. Two functions parametrize the nucleon structure in this regime, $F_1(Q^2)$ and $F_2(Q^2)$, the Dirac and Pauli form factors, respectively. F_1 is related to the charge distribution in the nucleon and F_2 accounts for the presence of an anomalous magnetic moment in the nucleon [5]. In the limit $Q^2 \to 0$, where the lepton probe sees the nucleon as a whole, the following relations hold for the neutron and the proton:

$$\begin{matrix} F_1^n(0) = 0 & F_2^n(0) \approx -1.9\mu_N \\ F_1^p(0) = 1 & F_2^p(0) \approx 1.8\mu_N \end{matrix} \qquad (3)$$

Since the proton has unit charge and the neutron has zero, F_1 is unity and zero for these systems, respectively. The magnetic moment of a point-like proton, in this Q^2 limit is expected to be unity, as it should be related to the charge distribution. By a similar argument, it is expected to be zero for a point-like neutron. Thus the discovery of the anomalous magnetic moments of the nucleons was a strong indication that nucleons were not elementary. F_1 is related to the electromagnetic charge density in the the transverse plane of an unpolarized nucleon through a Fourier transform [5]:

$$\rho(b_\perp) = \int \frac{d^2q}{2\pi} e^{(iq.b_\perp)} F_1(Q^2), \qquad (4)$$

where $b_\perp$ is an impact parameter representing the transverse distance of a parton from the center of mass of the nucleon. F_2 has a similar relation, but for a transversely polarized nucleon [5]. In this regime, the unpolarized cross section (Rosenbluth formula) is given by [5]:

$$\frac{d^2\sigma}{d\Omega} = \frac{\alpha^2}{4E^2 sin^4(\frac{\theta_e}{2})} \frac{E'}{E} \left\{ \left(F_1(q^2) - \frac{q^2}{4M^2} F_2^2(q^2) \right) cos^2(\frac{\theta_e}{2}) - \frac{q^2}{2M^2} \left(F_1(q^2) + F_2(q^2) \right)^2 sin^2(\frac{\theta_e}{2}) \right\} \quad (5)$$

Each of these two processes (inelastic and elastic scattering) lacks information contained in the other. The PDFs do not contain information about the spatial distribution of the contents of the nucleon whilst the Form Factors do not carry any information concerning the dynamics of the constituents. Therefore, none of them can provide a full picture of the nucleon's interior.

Combining the concepts of PDFs, Form Factors, and correlations between states of different longitudinal and transverse momentum dependence [17], the GPD framework provides a new tool to study nucleon structure. GPDs describe hadron structure in the non-perturbative region through Deep Exclusive Scattering(DES) processes. In the GPD framework, the corresponding factorizing structure functions are the GPDs $H(x, \xi, t)$, $E(x, \xi, t)$, $\tilde{E}(x, \xi, t)$ and $\tilde{H}(x, \xi, t)$ [7], at leading order and leading twist. The GPDs correspond to the amplitude of removing, from the nucleon, a parton of momentum fraction $x + \xi$ and restoring it back with momentum fraction $x - \xi$ [9], as shown in Fig. 1. Depending on the kinematics of the experiment, the parton can either be a quark or a gluon. In this framework, x represents the longitudinal momentum fraction of the nucleon carried by a parton. ξ, the skewness parameter, represents the longitudinal fraction of the momentum transfer to the nucleon($\Delta_{||}$).

t ($= \Delta^2$) is the squared 4-momentum transfer between the initial and the final nucleon, $\Delta = p' - p$ ($= \Delta_{||} + \Delta_{\perp}$) in Fig. 1. Since t is not a longitudinal parameter like x and ξ, it takes into account that there can also be a transverse component of the momentum transfer [7].
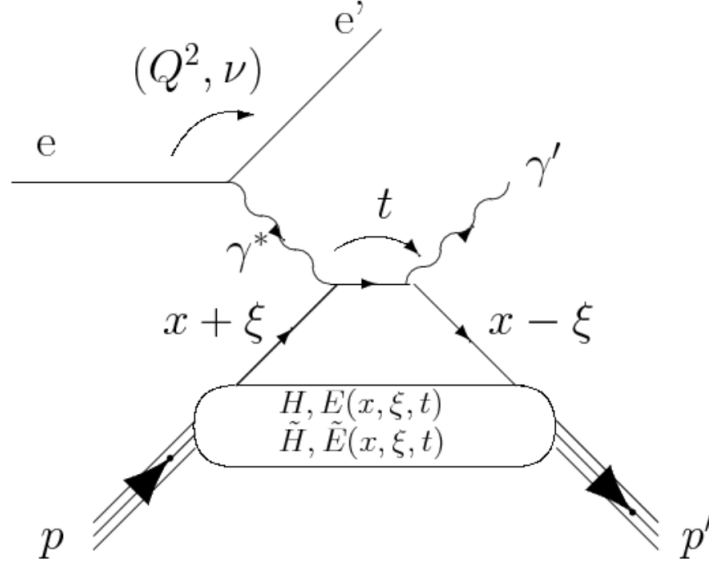

Figure 1: The "Handbag" diagram for DVCS. The momentum four-vectors of the incident and scattered electron are e and e', respectively. The momentum four-vectors of the virtual (incident) and real (scattered) photon are represented by γ^* and γ. t is the invariant momentum transfer to the nucleon which has initial and final momentum four-vectors p and p'. ξ is the longitudinal momentum fraction transferred to the nucleon and x is the longitudinal momentum fraction carried by a struck parton. The functions H, $\tilde{H}$, E and $\tilde{E}$ are GPDs factorizing the strong interactions in DES, as explained in the text. Figure taken from [7].

The Fourier transform of the GPDs with respect to the transverse component of the momentum transfer, $\Delta_{\perp}$ is related to the transverse position $b_{\perp}$, which gives the transverse spatial distribution of partons as a function of x. This enables GPDs to combine the spatial information with the longitudinal momentum information to give a 3-D picture of the interior of the nucleon, as shown in figure 2.

Since the GPDs unify a wealth of information, their moments in the momentum fraction x integrates out some kinematic dependencies and takes us back to a 2-D representation of the nucleon's interior. The first moments of the GPDs simplify to the elastic form factors [17]:

$$\int_{-1}^{+1} dx H^q(x,\xi,t) = F_1^q(t) \quad \int_{-1}^{+1} dx E^q(x,\xi,t) = F_2^q(t)$$
$$\int_{-1}^{+1} dx \tilde{H}^q(x,\xi,t) = g_A^q(t) \quad \int_{-1}^{+1} dx \tilde{E}^q(x,\xi,t) = h_A^q(t),$$

(6)

where F_1^q and F_2^q are the electromagnetic Dirac and Pauli form factors, respectively. g_A^q is the axial form factor and h_A is the pseudoscalar form factor. The second moment of the GPDs is related to the spin structure of the nucleon. According to a gauge-invariant nucleon spin decomposition by Ji [10], the spin can be broken down into:

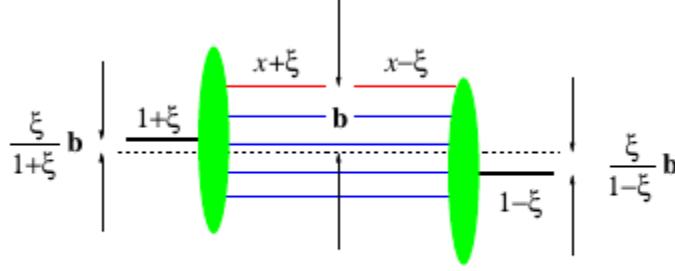$$\frac{1}{2} = J = J^q + J^g$$

(7)

7

Figure 2: Representation of a GPD in impact parameter space. In the plane transverse to the direction of a fast moving nucleon, a GPD (the blue blob), represents the wavefunction of an incoming and outgoing nucleon. In impact parameter space, the GPD probes partons at spatial parameter **b**. The initial and final nucleon states are shifted from each other by an amount of order ξ**b**. Figure taken from [8].

In equation 7, J^q is the contribution of the total angular momentum of quarks to the nucleon spin and J^g is a similar contribution from the gluons. The quark contribution can be decomposed further as:

$$J^q = \frac{1}{2}\, \Delta\, \Sigma + L_q, \tag{8}$$

where $\frac{1}{2}\Delta\Sigma$ is the spin part and L_q is the orbital angular momentum part. The second moment of the GPDs, evaluated at zero momentum transfer ($t = 0$), is then related to J^q via Ji's sum rule [10]:

$$J^q = \frac{1}{2}\int_{-1}^{+1} dx x[H^q(x,\xi,t=0) + E^q(x,\xi,t=0)]$$
$$= \frac{1}{2}\Delta\Sigma^q + L^q \tag{9}$$

With the spin contribution ($\Delta\Sigma^q$) measurable in DIS experiments, this means measuring the second moment of the GPDs can, via the sum rule, determine the quark orbital momentum contribution to the nucleon spin. This field is still in its infancy and if these connections exist, a lot is still to be done before the nucleon spin can be unpacked using this approach.

II.II Measuring GPDs via DVCS

Electroproduction of a photon can occur through two processes. The Bethe-Heitler(BH) is a process where the photon is emitted along one of the electron lines, before or after the interaction vertex, as shown in figure 3. This process is completely calculable if one knows the nucleon form factors. The photon can also be emitted by the nucleon(from this point on, the nucleon under study is specifically a proton) and this is the DVCS process. The total cross section beyond leading twist is given by [1]:

$$\frac{d\sigma^{ep\rightarrow ep\gamma}}{dQ^2 dx_B d\phi_e dt d\phi} = \frac{\alpha^3 x_B y}{16\pi^2 Q^2\sqrt{1 + 4x_B^2 M^2/Q^2}}\left|\frac{\mathcal{T}}{e^3}\right|^2 \tag{10}$$

8

Besides the photon virtuality Q^2 and the momentum transfer t, the cross section also depends on the DIS scaling(Bjorken) variable $x_B = Q^2/(2M_p\nu)$, where $\nu = E - E'$ is the electron energy transfer. It also depends on the fraction of the electron energy lost in the nucleon rest frame, $y = \frac{\nu}{E}$, the electron azimuthal angle with respect to the horizontal plane, around the beam-line direction, ϕ_e, the angle between the leptonic plane and the hadronic plane, ϕ, as shown in Fig. 4.

DVCS   BH
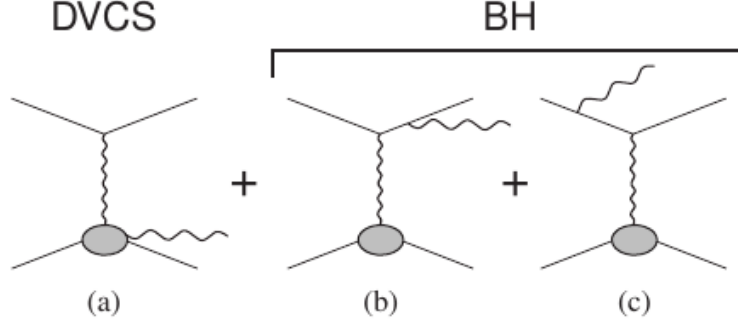
(a)   (b)   (c)

Figure 3: Mechanisms that can lead to electroproduction of a real photon, (a) DVCS process, (b) and (c) Bethe-Heitler process diagrams. The figure was taken from [17].

Since the DVCS amplitude interferes with the BH one, this results in a total amplitude, $\mathcal{T}$, which is a superposition of the BH and DVCS amplitudes, see Fig. 3.

$$
\begin{aligned}
|\mathcal{T}|^2 &= |\mathcal{T}_{\mathcal{DVCS}}|^2 + |\mathcal{T}_{\mathcal{BH}}|^2 + \mathcal{I} \\
\mathcal{I} &= \mathcal{T}_{\mathcal{DVCS}}^\dagger \mathcal{T}_{\mathcal{BH}} + \mathcal{T}_{\mathcal{BH}}^\dagger \mathcal{T}_{\mathcal{DVCS}}
\end{aligned}
\tag{11}
$$

where $\mathcal{T}_{\mathcal{BH}}$ and $\mathcal{T}_{\mathcal{DVCS}}$ are the BH and DVCS amplitudes respectively. $\mathcal{I}$ is the interference between the BH and DVCS processes. The cross section is proportional to the square of the amplitude, with the contribution from the DVCS process containing information about the GPDs and the BH contribution encoding Form Factor information. The terms contributing to the amplitude($\mathcal{T}_{\mathcal{BH}}$, $\mathcal{T}_{\mathcal{DVCS}}$ and $\mathcal{I}$) can be expanded into finite sums of Fourier harmonics, where different terms of the sum correspond to different twist levels (twist-two, twist-three, etc.). A calculation at a twist level can be defined as a suppression of the amplitude by powers of $\frac{1}{Q^2}$ [1]. Refs.[16] presents the BH, DVCS and interference harmonic expansions as:

$$
|\mathcal{T}_{\mathcal{BH}}|^2 = \frac{e^6}{x_B^2 y^2 (1+\epsilon^2)^2 \Delta^2 \mathcal{P}_1(\phi)\mathcal{P}_2(\phi)} \left\{ \mathcal{C}_0^{BH} + \sum_{n=1}^{2} \mathcal{C}_n^{BH} cos(n\phi) + \mathcal{S}_1^{BH} sin(\phi) \right\}
\tag{12}
$$

$$
\mathcal{I} = \frac{\pm e^6}{x_B y^3 \Delta^2 \mathcal{P}_1(\phi)\mathcal{P}_2(\phi)} \left\{ \mathcal{C}_0^{\mathcal{I}} + \sum_{n=1}^{3} [\mathcal{C}_n^{\mathcal{I}} cos(n\phi) + \mathcal{S}_n^{\mathcal{I}} sin(n\phi)] \right\}
\tag{13}
$$

$$
|\mathcal{T}_{\mathcal{DVCS}}|^2 = \frac{e^6}{y^2 Q^2} \left\{ \mathcal{C}_0^{DVCS} + \sum_{n=1}^{2} [\mathcal{C}_n^{DVCS} cos(n\phi) + \mathcal{S}_n^{DVCS} sin(n\phi)] \right\},
\tag{14}
$$

where the $(\pm)$ in the interference term represents a sign convention for negatively(-) and positively(+) charged lepton probes. Furthermore, $\mathcal{P}_1(\phi)$ and $\mathcal{P}_2(\phi)$ are the BH electron propagators

9

expressed as [17];

$$Q^2\mathcal{P}_1 = (k - q')^2 = Q^2 + 2k\Delta, \tag{15}$$

$$Q^2\mathcal{P}_2 = (k - \Delta)^2 = -2k\Delta + \Delta^2, \tag{16}$$

with q' and k representing the virtual photon and the incoming electron 4-vectors, respectively.

It is worth noting that even though the GPDs depend on three variables x, ξ and t, the variable x is not experimentally accessible as a result of the closed loop in the DVCS process. GPDs, therefore, can not be measured directly in an experiment. Instead, Compton Form Factors(CFF), which depend on two variables, ξ and t can be measured. The connection between the experimental observables containing GPDs(that is to say, CFFs) and the DVCS amplitude is carried by the coefficients of the expansion terms of the Fourier harmonics (see equations 12, 13 and 14). The $\mathcal{C}$'s are functions of the CFFs, which are integrals of the GPDs.

Since the GPDs encode helicity information, they can be toggled using beam-target spin degrees of freedom. Thus the use of polarized beams and or targets allows access to different linear combinations of GPDs, depending on the choice of polarization configuration. In this case, one can either calculate the total (unpolarized) cross section or a helicity correlated difference of cross sections. For polarized experiments (either beam or target or both polarized), the difference of cross sections are sensitive to BH-DVCS interference terms [7], giving a linear combination of the electromagnetic Form Factors F_1, F_2 and the CFFs. According to Ref. [7], in general, single spin observables (either beam or target polarized, but not both) are sensitive to the imaginary part of the CFFs while double spin observables (both beam and target polarized) are sensitive to real part of the CFFs. The total(unpolarized) cross section is sensitive to the real part. Reference [18] summarizes this using equations 17:

$$d\vec{\sigma} - d\vec{\sigma} = 2 \cdot \mathcal{T}_{\mathcal{BH}} \cdot Im(\mathcal{T}_{\mathcal{DVCS}}) + [|\mathcal{T}_{\mathcal{DVCS}}^{\rightarrow}|^2 - |\mathcal{T}_{\mathcal{DVCS}}^{\leftarrow}|^2]$$
$$d\vec{\sigma} + d\vec{\sigma} = |\mathcal{T}_{\mathcal{BH}}|^2 + 2 \cdot \mathcal{T}_{\mathcal{BH}} \cdot Re(_{\mathcal{DVCS}}) + |\mathcal{T}_{\mathcal{DVCS}}|^2 \tag{17}$$

with the arrows representing either a polarized target or a polarized beam.

It is also interesting to note that different targets give different access to the GPDs. Furthermore, for the same target, different target-beam spin orientations will give access to different linear combinations of the GPDs. In particular, the difference of polarized cross sections on a neutron target is understood to access a linear combination of GPDs in which the GPD E dominates. Since the GPD E is one of the arguments into Ji's sum rule, this makes the neutron an interesting lab for future DVCS experiments. Since free neutrons can not last the duration of these experiments, a simple neutron-proton bound state would be useful. Due to its spin structure, polarized ^{3}He is the ideal source of free, polarized neutrons and is promising to be the focus for future DVCS experiments.

II.III Existing DVCS Measurements

Since the last decade, DVCS cross sections have been measured in two distinct kinematic regimes: the quark-gluon sea, at low x_B, and the valence region at higher x_B, as shown in Fig. 5.

The HERA collider was one of the pioneer DVCS experiments. At HERA, the H1 and ZEUS collaborations operated with 27.5 GeV positrons and 820 GeV protons at center of mass energy 30<W<130 GeV and 8<Q^2 <85 GeV^2[4]. They measured the unpolarized cross section of the $ep \rightarrow ep\gamma$ process.
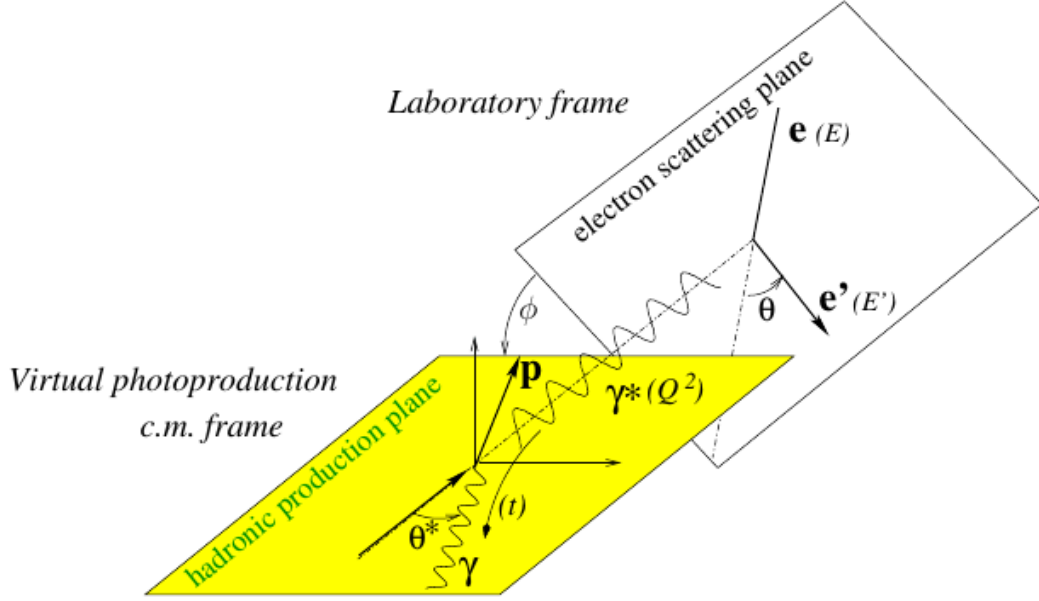
Figure 4: Description of reference frames for the DVCS reaction, according to the Trento convention. Figure was taken from [7].

At such high energies (low x_B) the DVCS process is sensitive to the quark-gluon sea, hence gluon GPDs.

At HERMES, an electron beam as well as a positron beam was used to measure DVCS beam asymmetries, longitudinally and transversely polarized target asymmetries, beam-charge asymmetries and all associated beam-spin/target-spin/beam-charge double asymmetries [7]. The average kinematics at HERMES were $< Q^2 > = 2.6$ GeV^2, $< x_B^2 > = 0.11$ and $< -t > = 0.27$ GeV^2, using a 27.5 GeV positron/electron beam. At leading twist, DVCS asymmetries and moments are understood (from theory) to vanish. Results from the HERMES data were found to be in agreement with theory, within error bars[7]. This agreement, in a small band in Q^2, is a strong sign of the dominance of the handbag diagram over higher twists.

The Hall B collaboration (CLAS) at TJNAF also measured beam spin asymmetries at average kinematics $< Q^2 > = 1.25$ GeV^2, $< x_B^2 > = 0.19$ and $< -t > = 0.19$ GeV^2, using a 4.2 GeV electron beam. A 20 - 30 % asymmetry was observed. The asymmetries indicate a $\sin\phi$ behavior, which is in agreement with theoretical models. This agreement suggest sensitivity to the handbag description of the DVCS process and an indication that the GPD formalism might be a valid description of nucleon structure.

The TJNAF Hall A collaboration measured both unpolarized and the difference of polarized cross sections with W$\approx$2 GeV, using an electron beam on a fixed proton target. Four-fold beam-polarized and unpolarized cross sections were measured, $d^4\sigma/dx_B dt d\phi dQ^2$. Measurements were done at four values of $-t$: 0.17,0.23, 0.28 and 0.33 GeV^2 for kinematics $< x_B > = 0.36$ and $< Q^2 > = 2.3$ GeV^2. In addition, beam polarized cross sections were measured at $< Q^2 > = 1.5$ GeV^2 and $< Q^2 > = 1.9$ GeV^2. These data have played a significant role to provide constraints in extracting the real and imaginary parts of the GPD H[5]. Early conclusions show that the valence quarks (high x) seem to
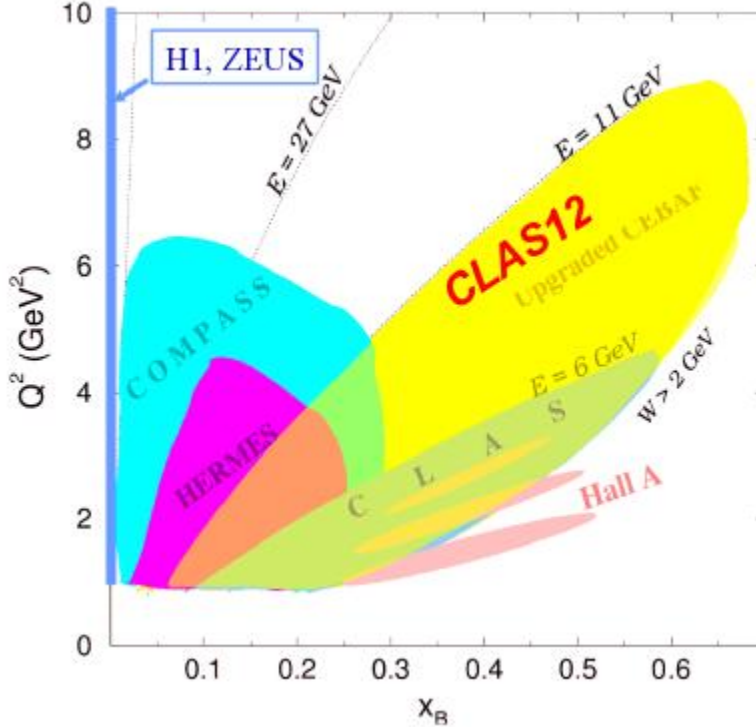
Figure 5: The kinematic domain,Q^2 as a function of x_B for past (H1, ZEUS, HERMES, TJNAF at 6 GeV) and future (COMPASS, TJNAF at 12 GeV) DVCS measurements. Figure was taken from Ref. [5].

remain at the center of the nucleon while the sea and gluons (low x) can extend towards the "surface" of the nucleon. CFFs have also been extracted from this data, indicating early scaling properties.

These results have shown early signs of validation of the GPD formalism and the handbag picture of DVCS but are limited to a narrow kinematic region, small Q^2 (less than or equal to 2.3 GeV^2) and x_B (less than or equal to 0.36). The proposed thesis work presented by this document intends to explore a wider range in both Q^2 and x_B, thus testing the precision with which the handbag amplitude dominates (or does not) over higher twist amplitudes. This will be made possible by the new (and wide, x_B up to 0.6 and Q^2 up to 9 GeV^2) kinematic region availed by the 12 GeV era at the TJNAF. Future DVCS experiments in Hall B and Hall C will also explore previously non-explored regions. At CERN, COMPASS is set up to study DVCS at the sea quark and gluon regime (at very low x_B). All these efforts will contribute to constrain existing GPD models even further and extracting with confidence, nucleon information in the GPD formalism.

II.IV GPD Models

Together with experimental data, models of the nucleon structure are a fundamental tool in the exploration of nucleon structure and the dynamics of QCD in the non-perturbative domain. Different kinds of models have been developed to interpret experimental data for exclusive processes like DVCS. A brief description of the models used in the recent literature is presented in this section.
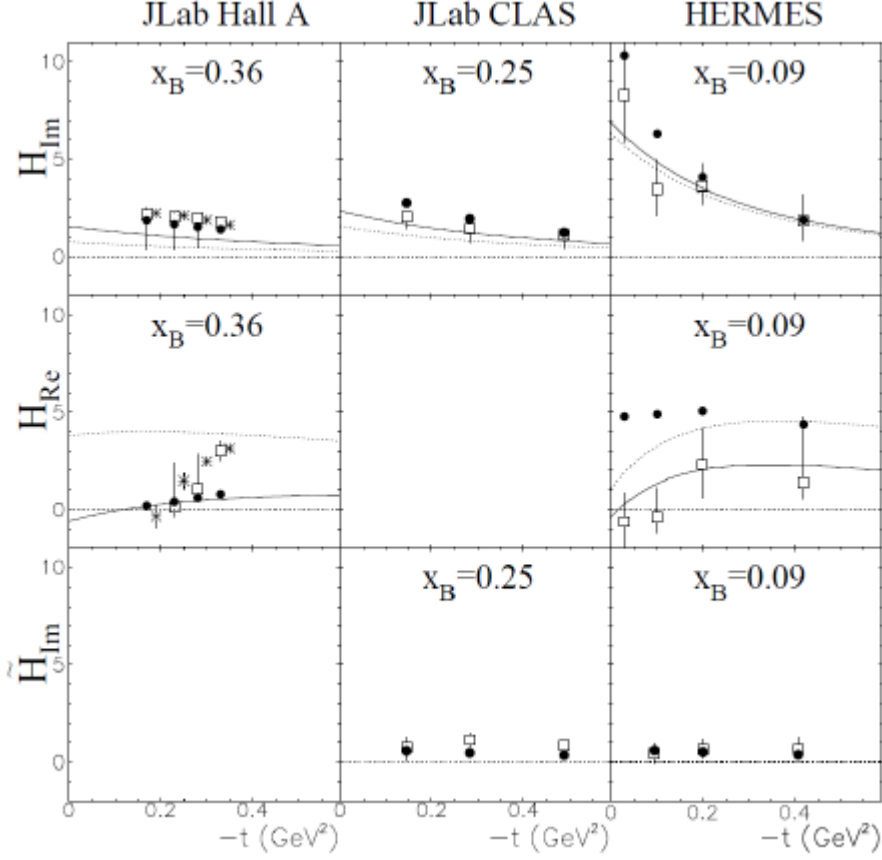
Figure 6: The real and imaginary CFFs H and $\tilde{H}$ as a function of -t. Empty plots are fits of CFF fit using TJNAF and HERMES data. The solid points show predictions of the VGG model of GPDs. Figure was taken from Ref. [5].

II.IV.1 Double Distribution (DD) Models

In the valence region, the most widely used models are based on the Double Distribution Ansatz proposed by A. Radyushkin[12] and D. Muller[13]. The DD functions parametrize the x and ξ dependence of the GPDs in terms of momentum fractions β and α of P$^+$ (average nucleon momentum)and Δ^+ (average momentum transfer to nucleon) respectively. In terms of the double distributions DD$^q(x,\xi)$, the GPD$^q(x,\xi)$ is expressed as[4]:

$$GPD^q_{DD}(x,\xi) = \int_{-1}^{+1} d\beta \int_{-1+|\beta|}^{1-|\beta|} d\alpha \, \delta(x - \beta - \alpha\xi) DD^q(\beta, \alpha). \tag{18}$$

The momentum fractions β and α linearly correlate x and ξ. The double distribution DD$^q(\beta, \alpha)$ can be interpreted as the probability amplitude to find a quark of momentum fraction β of the average proton momentum (between the initial and final state) and the fraction $(1+\alpha)/2$ of the momentum transfer Δ to the nucleon. The shape of this DD is restricted by two limits[5]:

1. At $\Delta = 0$ ($\xi = 0$), the process reduces to its forward limit ($t = 0$) giving us access to PDFs.

2. At $\Delta \neq 0$, in the limit of vanishing final proton momentum, the DDs are interpreted as the probability amplitude of finding (in the proton) a meson pair of distribution amplitude of the form $[(1 - \beta) - \alpha][(1 + \beta) + \alpha)]$ [11].

13

Therefore, the parametrization of the DDs must include the PDFs (in the limit $\Delta = 0$) and meson Distribution Amplitudes (in the limit P=0). Such a parametrization can be written as:

$$DD^q(\beta,) = h(\beta, \alpha)q(\beta) \tag{19}$$

where $q(\beta)$ is the parton distribution function and $h(\beta, \alpha)$ is a profile function defined as [5]:

$$h(\beta, \alpha)q(\beta) = \frac{\Gamma(2b+2)}{2^{2b+1}\Gamma^2(b+1)} \frac{[(1 - |\beta|) - \alpha^2]^2}{(1 - |\beta|)^{2b+1}}. \tag{20}$$

b is a free parameter that gives the strength of the dependence of the GPDs on ξ.

II.IV.2 The Dual Model

In this model, GPDs are expanded in terms of the partial waves exchanged in the t-channel. In a similar fashion to electric and magnetic combinations of form factors, the t-channel partial waves are described by the GPD combinations [11]:

$$H^{(E)}(x, \xi, t) = H(x, \xi, t) + \frac{t}{4M^2} E(x, \xi, t) \tag{21}$$

$$H^{(M)}(x, \xi, t) = H(x, \xi, t) + E(x, \xi, t) \tag{22}$$

The dual distribution is also introduced for the charge singlet and non-singlet combinations $H_+^{(E,M)}$ [11]:

$$H_+^{(E,M)} = H^{(E,M)}(x, \xi, t) - H^{(E,M)}(-x, \xi, t) \tag{23}$$

The partial wave decomposition of the electric singlet GPD H_+^E is given by

$$H_+^E(x, \xi, t) = 2 \sum_{n=1,odd}^{\infty} \sum_{l=0,even}^{n+1} B_{nl}^{(E)} \theta(1 - \frac{x^2}{\xi^2})(1 - \frac{x^2}{\xi^2}) C_n^{\frac{3}{2}} P_l(\frac{1}{\xi}), \tag{24}$$

where l represents an orbital angular momentum exchange in the t-channel, $C_n^{\frac{3}{2}}$ are Gegenbauer polynomials, P_l are Legendre polynomials and B_{nl} are generalized form factors [11].

II.IV.3 The Mellin-Barnes Model

Similar to the dual model, the Mellin-Barnes model is based on a partial wave expansion of GPDs. The difference between the dual and the Mellin-Barnes models is the technique used to sum the partial wave expansion series. In the Mellin-Barnes model, conformal moments of a GPD are defined as [11]:

$$F_n(\xi) = \int_{-1}^{1} dx c_n(x, \xi) F(x, \xi), \tag{25}$$

where c_n are Gebenbauer polynomials. The conformal partial wave expansion can be written as:

$$F(x, \xi) = \sum_{n=0}^{\infty} (-1)p_n(x, \xi) F_n(\xi), \tag{26}$$

where p_n are polynomials orthogonal to c_n. The final parametrization of GPDs yields the following expression [11]:

$$H(\xi, \xi, t) = \frac{nr}{1 + xi} \left(\frac{2\xi}{1+\xi}\right)^{-\alpha(t)} \left(\frac{1-\xi}{1+\xi}\right)^b \frac{1}{(1 - \frac{1-\xi}{1+\xi}\frac{t}{M^2})^p}, \tag{27}$$

14

where n, $\alpha(t)$ and p are free parameters.

II.V   Extracting GPDs from data

The ultimate goal of these experiments is to extract a set of observables that we can model and use in understanding nucleon structure through the DVCS process. Fitting GPDs from experimental data is a much involved process since it entails the extraction of four functions H, E, $\tilde{H}$ and $\tilde{E}$ (at leading order and leading twist) of three variables (x, ξ, t) for each quark flavor (u, d, s)[11]. A brief description of the fitting methods used in the current literature is presented below.

- Local fits of CFFs:
  This method is based on the assumption that the real and the imaginary parts of the CFFs are independent of each other. Another assumption is the dominance of the twist-2 leading order term in the DVCS amplitude together with a weak contribution by the CFF Im $\tilde{\mathcal{E}}$. To extract the CFFs as a function of ϕ (i.e fitting the coefficients $\mathcal{C}_n$ of equations 13 and 14), the data is split into different 3D kinematic bins (x_B, t, Q^2). Each bin is treated independently of the others and seven CFFs Re $\mathcal{H}$, Im $\mathcal{H}$, Re$\mathcal{E}$, Im $\mathcal{E}$, Re $\tilde{\mathcal{H}}$, Im $\tilde{\mathcal{H}}$ and Re $\tilde{\mathcal{E}}$ are extracted simultaneously. The good thing about this method is that it is almost model-independent, however, it is often under-constrained [11]. Moreover, with this method, it is impossible to extrapolate outside the data region.

- Global fits of GPDs:
  For each experimental data set, this method deals with all observables in all kinematic bins at once. It is very useful in extrapolating outside the data region and hence more suited to the study of the 3D partonic structure of the nucleon. Even though most global fits are based on a leading order assumption for the DVCS process, there has been a recent emergence of calculations at next to leading order.

- Other fitting techniques:
  Hybrid fits are a combination of both local and global fits and assumes the dominance of the GPD H together with twist-2 dominance.
  Neural network fits of GPDs have been used successfully used for PDFs but their use for GPDs is quite new. Results with the H-dominance assumption have been described and presented in recent literature. Since it's usage is new for GPDs, this method's pros and cons are not well know yet.

Up to this point, global fits have been used to extract the GPDs H_{Im} and $\tilde{H}_{Im}$ [7] from the existing data. Even though the fitting method has many assumptions (hence limitations), it has the benefits of showing the transverse size of the proton as a function of x_B (see Fig. 7). With the 12 GeV upgrade of the TJNAF, new high precision data over a wider range phase space factor is projected to make it possible to extract all leading twist CFFs.
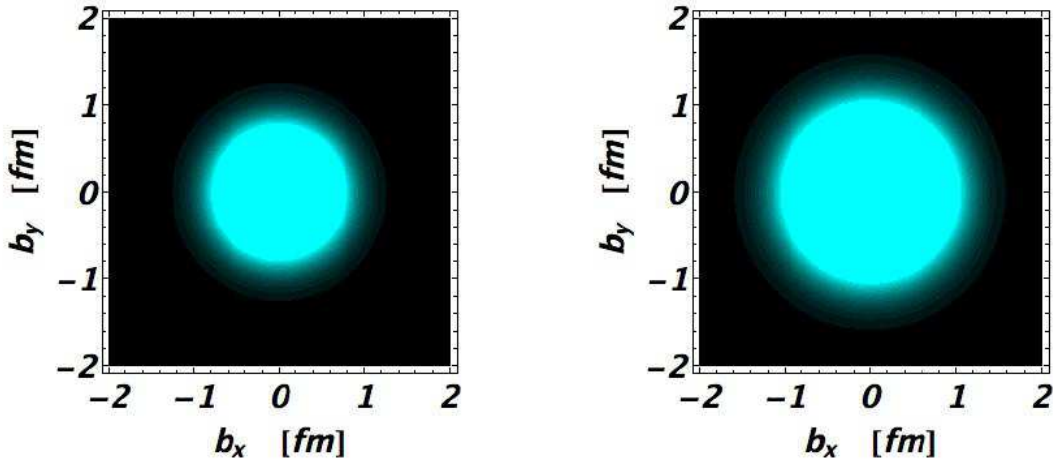
Figure 7: Contour plots of the spatial charge density from global fitting by Ref.[7] for DVCS data. The cyan and black colors represent positive and negative charge, respectively. Interpretation of the data shows the proton as a positively charged center with negative tails, suggesting a negative pion cloud at the periphery of a positive center. Left panel: using CLAS data at $x_B = 0.25$, probing valence quarks. Right panel: using HERMES data at $x_B = 0.09$, probing the quark-gluon sea. It is interesting to note that when probed at different wavelengths, the size of the proton is appears different also. The figure was taken from [7].

III   Overview of Experiment E12-06-114

Experiment E12-06-114 will use exclusive electron scattering to measure helicity-dependent and helicity-independent cross sections for the DVCS ($ep \rightarrow ep\gamma$) process off a proton target. The experiment will be conducted in the Hall A of the Thomas Jefferson National Accelerator Facility(TJNAF). Longitudinally polarized electron beams of 6.6, 8.8, and 11 GeV [1] will be fired to scatter off a 15 cm liquid hydrogen target. The scattered electrons will be counted using the left arm of Hall A's High Resolution Spectrometer. The produced DVCS photon will be registered using a 39 cm by 48 cm Lead-Fluoride(PbF_2) electromagnetic calorimeter. The recoil proton is not measured but a missing mass reconstruction of the DVCS reaction will be used to distinguish DVCS events with an overall impurity less than 3% [18]. The experiment will focus on the kinematic range $Q^2 > 2$ GeV^2, W > 2 GeV and momentum transfer $-\Delta^2 \leq 1$ GeV^2 [18]. The projected kinematic coverage of the experiment is shown in Fig. 8.

   Experiment Goals
The principal goal of the experiment is to measure precise helicity-dependent and helicity-independent cross section of the DVCS process, which is related to the CFFs. This will be done at fixed kinematic points x_B over a large range in Q^2. Once measured, absolute cross sections will be useful in revealing many properties about the proton system, such as:

  • Scaling tests of DVCS cross sections. Scaling is the property that the proton's structure functions do not have a Q^2 dependence at leading twist. Earlier DVCS experiments confirmed the scaling

―――――――――――――――――――――
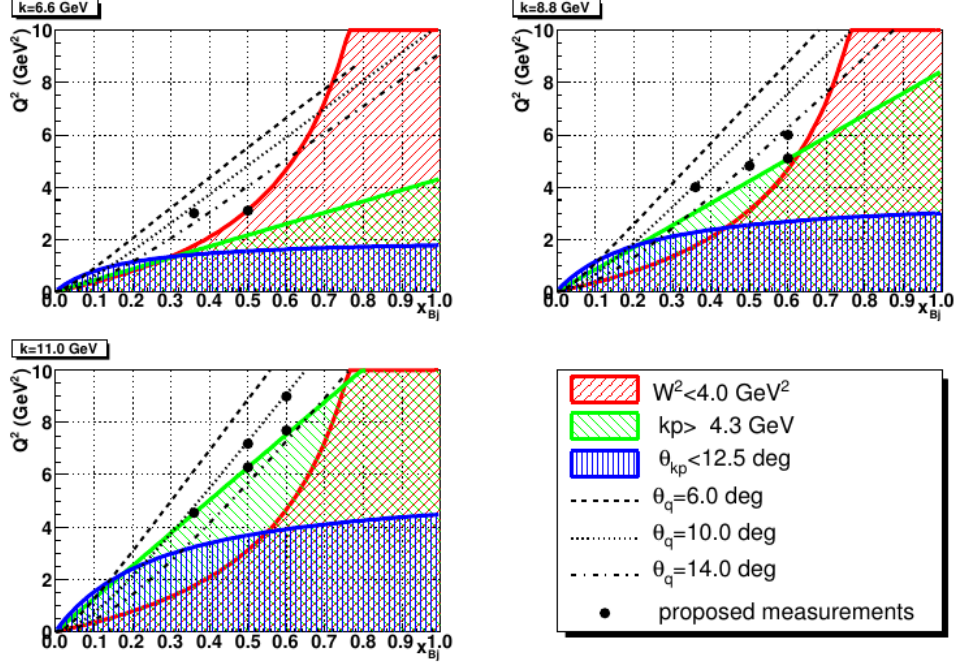
[1]These are nominal energies

Figure 8: Proposed DVCS central kinematics for the upcoming experiment E12-06-114. kp represents the scattered electron momentum, θ_{kp} is the angle of the scattered electron. θ_q is the angle of the real photon and W is the invariant mass of the virtual photon-proton system. The region shaded in red represents the elastic and resonance region. Shaded in green is the region where the scattered electron momentum is above the maximum central momentum of the spectrometer. In blue is the region below the minimum angular acceptance of the spectrometer from the beam line. The spectrometer can come as close as 12.5^o to the beam line. The calorimeter will be placed between the beam line and the right arm of the spectrometer. The closest it can be to the beam line is 6°. This figure is Reproduced from [18].

property but over a narrow range in Q^2 (between 1.4 and 2.4 GeV^2 [7]). Experiment E12-06-114 will test the scaling property for a Q^2 range between 3 and 9 GeV^2. Passing this test will prove that the GPD formalism is appropriate to describe nucleon structure.

- To separately measure the Real and Imaginary parts of the DVCS amplitude. The angular harmonics which are sums of CFFs (and FFs) enable access to the Real and Imaginary parts of different combinations of CFFs and FFs. Therefore, a precise measurement of cross section will lead to improved knowledge of Real and Imaginary amplitudes of the DVCS and BH process.

- The 12 GeV upgrade also comes with the advantage for large kinematic coverage in Q^2, x_B and t. A wide kinematic range is necessary to map out the proton at many points and provide data that will be useful in extracting GPD parametrizations. Such measurements are likely to improve current GPD models and eventually reduce the model dependence of the GPD parametrizations. The new(12 GeV) Q^2 range compared to the 6 GeV range is shown in Fig. 9.

- Measurement of $e\vec{p} \rightarrow ep\pi^0$ cross section. This will test the factorization dominance of meson electro-production.
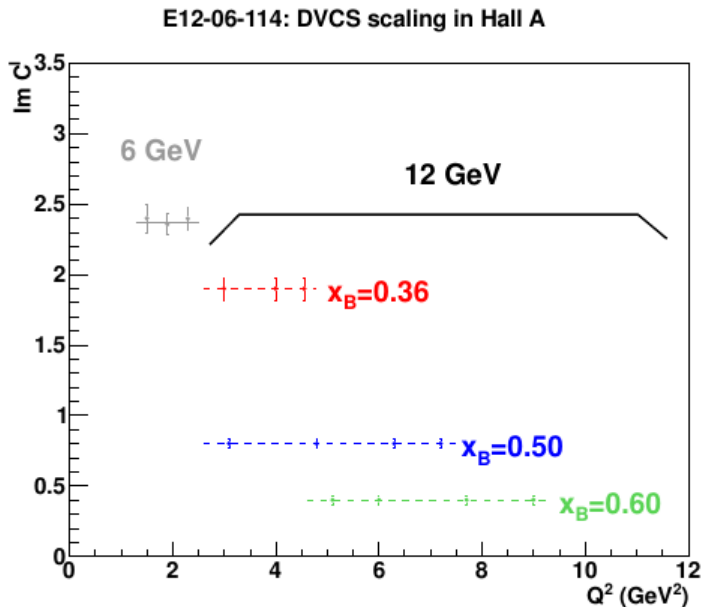
17

Figure 9: DVCS scaling in Hall A of TJNAF. The Q^2 domain possible with the 6 GeV beam is shown in gray and the domain that comes with the 12 GeV beam is shown in black. Also shown are the possible x_B variables that can be explored. This figure was taken from [7].

III.I The Continuous Electron Beam Accelerator Facility(CEBAF)

The CEBAF at the TJNAF produces polarized electron beams and recently got an upgrade from a possible maximum beam energy of 6 GeV to 12 GeV, after five passes. The accelerator has two superconducting linacs, North and South, connected by arcs with steering magnets to guide the electron beam from one linac to the other. CEBAF is designed to supply a continuous instead of a pulsed beam. This is made possible by the use of superconducting radio frequency technology which uses liquid helium to cool niobium cavities to about 4 K. At this temperature, the cavities lose electrical resistance, leading to a very efficient energy transfer to electrons.

To extract electrons, a gallium arsenide (doped with phosphorus) cathode (GaAsP) is hit with a laser, resulting in photoemission [19]. Beam polarization is achieved by polarizing a photon beam(laser) used to extract the electrons from the GaAsP cathode. The photons are passed through a voltage controlled wave plate, which polarizes the photons circularly[19]. Changing the sign of the voltage applied to the wave plate switches the sense of polarization($\pm$). A maximum of 85% beam polarization can be achieved[19].

The extracted electrons are accelerated up to 45 MeV before being injected into the North linac as demonstrated in Fig. 10 . The upgrade will see the electrons being accelerated to 1.1 GeV maximum energy in one linac. At the end of the first linac, the beam is bent into the South linac where it is again accelerated. This makes one pass. The beam can now be extracted to experimental halls A, B and C or can be recirculated for a second pass, up to a maximum of 5 passes.
The three halls can receive beam of the different energies simultaneously. A new experimental hall (hall D) has been constructed with the 12 GeV upgrade. This hall (D) is located in such a way that it will receive beam that has been accelerated through one more linac than the beam to the

18

other halls. Through the 12 GeV upgrade, halls A, B, and C will receive a maximum of 11 GeV while hall D has half a pass more beam circulation and will receive the maximum 12 GeV. The maximum beam current is 200 μA and can be independently split and supplied to all halls at the same time.
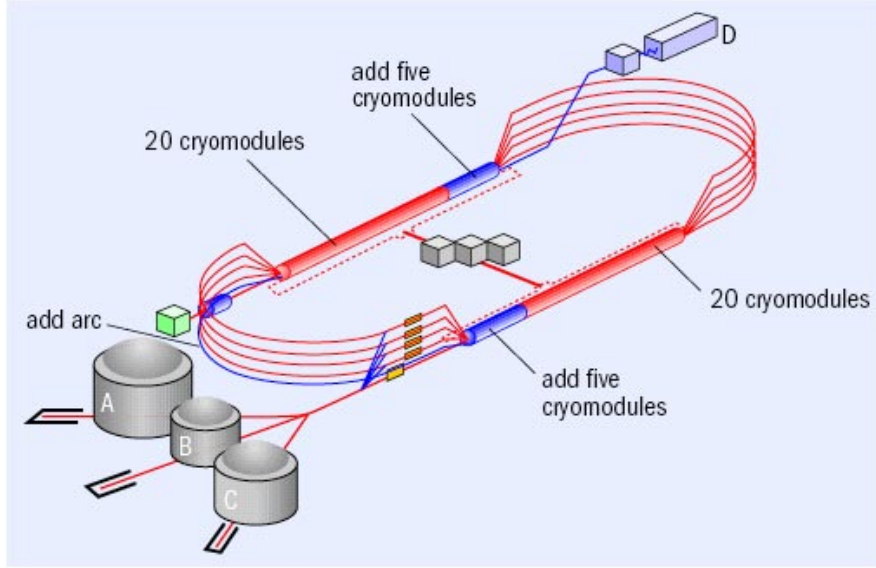

Figure 10: CEBAF with the 12 GeV upgrade. The injector is represented by the green box close to hall A and it is viewed by the North linac. The beam is injected into the North linac and passed to the South linac for a complete pass. The two linacs initially had 20 cyromodules each. With the 12 GeV upgrade, 5 cryomodules have been added to each linac and a new hall D has been installed in addition to the already existing halls A,B and C. The figure was reproduced from: https://www.jlab.org.

III.II   Experimental Hall A

The core components of Hall A are two identical High Resolution Spectrometers(HRS) used to detect scattered particles, for example, electrons. The layout of the hall is shown in Fig. 11. Upstream the target, several measurements of the properties of the beam are done. Two independent ways to measure beam polarization are installed. The Moller Polarimeter monitors the polarization of the beam by measuring the rate of production of Moller electrons at 90° when the beam hits a solid target, usually iron. Besides the Moller, the Compton polarimeter is also installed. Both polarimeters measure polarization to an accuracy of $\frac{\delta P}{P} \approx 3\%$[19]. These two detectors have been used redundantly to provide a systematic cross-check in the polarization measurement.

The hall is also equipped with Beam Current Monitors (BCMs) to determine the charge incident into the hall during a run. The BCMs are located upstream the target, between the polarimeters. Also located upstream is a raster system which is used to spread the beam out instead of being focused to almost a point. The beam can be rastered by several millimeters, usually 4 mm × 4 mm for cryogenic targets, both in the x and y directions perpendicular to the beam direction. The hall is also equipped with Beam Position Monitors (BPMs) to determine the position and direction of the beam at the target. The are two BPMs upstream, one 7.524 m and the other 1.286 m from the target. Using the BPMs, the beam position and angle can be determined to within 140 μm and 30 μrad[19].
Another property of the beam that is measured is the energy. For this, there are two methods. The

Arc method uses the deflection of the beam in the magnetic field of the arc to measure the absolute energy. This is achieved by measuring the integral of the magnetic field of the eight dipoles that steer the beam in the arc and the bending angle. The second method is called the eP method. It uses the scattered electron and the the recoil proton angles in the elastic scattering of electrons off a hydrogen target to determine the energy. The energy is measured with a $\frac{\delta E}{E} \approx 2 \cdot 10^{-4}$ precision.

Downstream the target, along the beamline, there is a tungsten beam dump to collect and contain the beam of unscattered electrons. Also located downstream are the two HRS, which are described next.
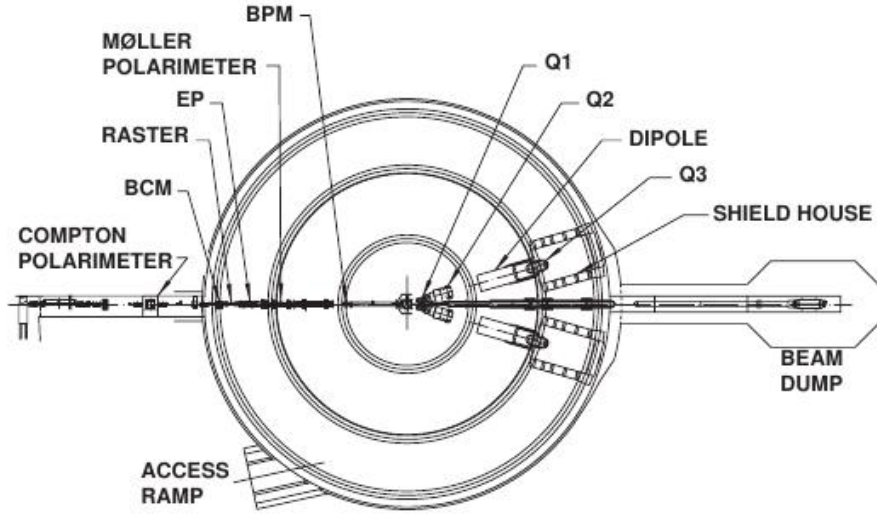

Figure 11: Cross section view of experimental hall A. Reproduced from [19]

The High Resolution Spectrometers(HRS)

The two identical spectrometers are abbreviated LHRS and RHRS for the left and right, respectively. Each spectrometer is made up of a detector package following three superconducting quadrupole magnets and one dipole magnet. The magnet configuration is shown in figure 12 and is known as the QQDQ configuration [19]. The quadrupoles are used to focus scattered charged particles as they are transported to the detectors in the hut. The dipole uses the bending of a charged particle in a magnetic field to determine its momentum. The spectrometers have a maximum central momentum 4.3 GeV. In the momentum range of 0.8 - 4.0 GeV, both spectrometers have a precision of $\frac{\delta P}{P} \approx 2 \cdot 10^{-4}$ and angular (horizontal) resolution better than 2 mrad. The transverse position resolution is approximately 1 mm, for both spectrometers.

The HRS Detector Package

A cartoon of the detector package is shown in figure 13, for the left arm. There is a similar setup for the right arm, with slight differences in the design of the component detectors. Each detector package is equipped with a pair of vertical drift chambers (VDC), a detector used to provide charged particle tracking by measuring the position and angle of the trajectory. The VDCs have a position resolution
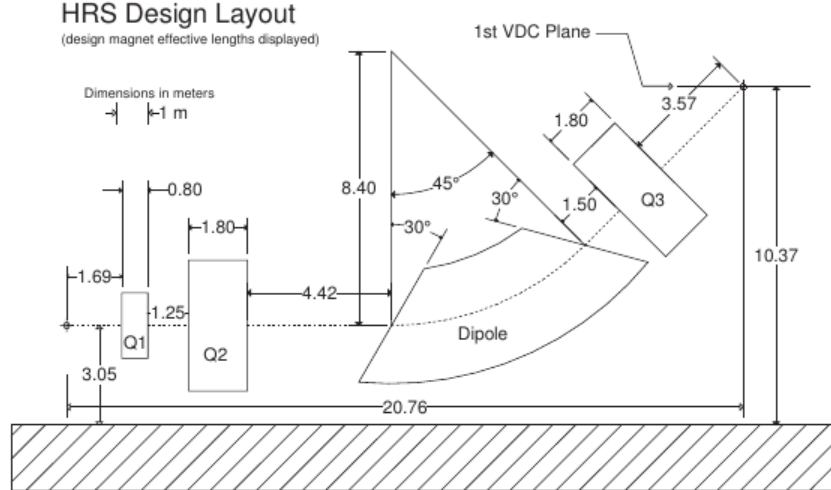
Figure 12: Cross section view of the HRS magnet setup. Reproduced from [19]

$\sigma_{x(y)} \approx 100$ m and angular resolution $\sigma_{\theta(\phi)} \approx 0.5$ mrad [19]. Besides tracking, the spectrometers are also equipped with detectors that provide a trigger, start data-acquisition (DAQ). Triggering is provided by two sets of scintillator paddles, S0 and S2m (S2 modified). S0 has one paddle and S2m has sixteen, each paddle being read by two photo-multipliers on either of its two ends. Also installed in the spectrometers are detectors for particle identification. For this reason, the gas Cherenkov detector is mounted between the S0 and the S2m and it provides particle identification by producing Cherenkov light in a carbon-dioxide environment at atmospheric pressure [19]. The detector allows electron identification with an efficiency above 99% and has a threshold of 4.8 GeV [19]. Particle identification is also provided by a set of two electromagnetic calorimeters (shower detectors). These are mounted after the S2m and are made of lead glass blocks to induce showers of pair production and bremsstrahlung radiation for a total collection of electron energy, while discriminating pions. Together with the gas Cheronkov detectors, the showers provide, on average, above 98% and a suppression factor of $2 \cdot 10^5$ for a pion of momentum above 2 GeV [19]. Both particle identification detectors can also be used to trigger DAQ, either in a single-detector mode or in coincidence with any other detector. This is the case for the DVCS experiment where the trigger will be provided by a coincidence of the gas Cherenkov and the S2m detectors, doing a trigger and particle identification simultaneously.

The target system

There is a scattering chamber which houses the various targets in use. The chamber is made of a 1cm thick spherical shell of aluminium. It houses both cryogenic and other (solid) targets.

Together with its cooling, gas handling, pressure and temperature monitoring sub-systems, the cryogenic target system is mounted inside the scattering chamber. Also inside the chamber are sub-systems for motion control and a solid target ladder. The cryogenic target has three independent loops: a liquid hydrogen (LH_2) loop, a liquid deuterium (LD_2) loop and a gaseous helium loop. For the E12-06-114 experimet, only the LH_2 is used. There is only one cylindrical aluminium target cell for the LH_2 loop. The target cell is 15cm and is mounted on the target ladder. The side-walls of the cell are 178μm while entrance and exit windows are 102 and 127μm thick, respectively. The target density is approximately 0.0723g/cm^3 as a result of an average operating pressure of approximately
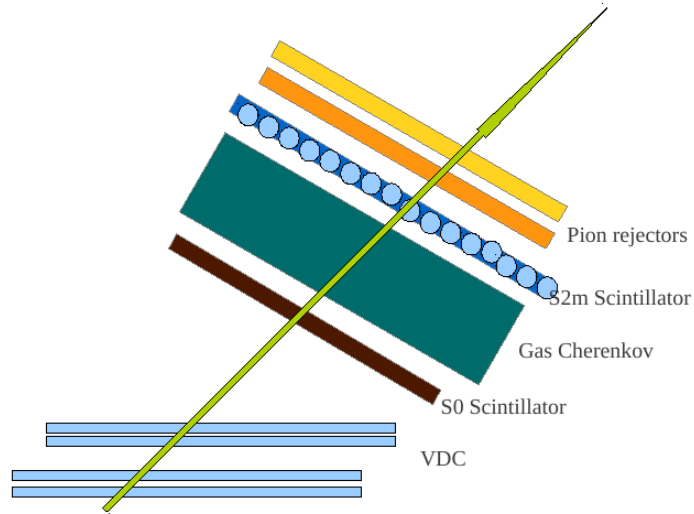
Figure 13: Cross section view of the HRS detector package. The arrow shows the nominal particle trajectory through the detector stack.

0.17MPa and temperature of 19K.

Besides the cryogenic target, there are also solid targets:

- Carbon: a 1mm thick sheet of carbon used for optics studies.

- BeO: is used to locate the beam spot at the target using a camera installed in the scattering chamber. It is very usefull when getting beam for the first time in a long while.

- Optics: a set of seven 1mm thick carbon sheets used for optics calibration of spectrometer.

- Dummy target: Aluminium foils used to study target wall effects.

- Empty: no target but a good position to place the target while beam is still being driven into the hall.

III.III The Electromagnetic calorimeter

The DVCS calorimeter is not part of the hall A standard equipment but part of the DVCS setup to detect the real photons produced during the DVCS process. It is made of 13×16 lead-fluoride (PbF_2) blocks each measuring $3 \times 3 \times 18.6$ cm^3. The calorimeter uses the electromagnetic shower principle to degrade the initial photon into secondary positron-electron pair showers. The secondaries then produce Cherenkov light which is collected by photo-multiplier tubes. Each PbF_2 block is viewed by one PMT. Properties of PbF_2 include:

- A large density (7.7 g/cm^3) making the detector very compact, hence a short radiation length (0.95 cm).

- Moliére radius of 2.22 cm providing approximately total energy absorption within 9 calorimeter blocks [1].

- Very fast rise time, total pulse width < 20 ns.

- Sufficient energy resolution, $\frac{\sigma_E}{E} \approx \frac{5.3}{\sqrt{(E(GeV))}}$ [18]

- Reasonable secondary photon yield, Monte-Carlo simulations estimate 1000 Cherenkov photons per 1 GeV [1].
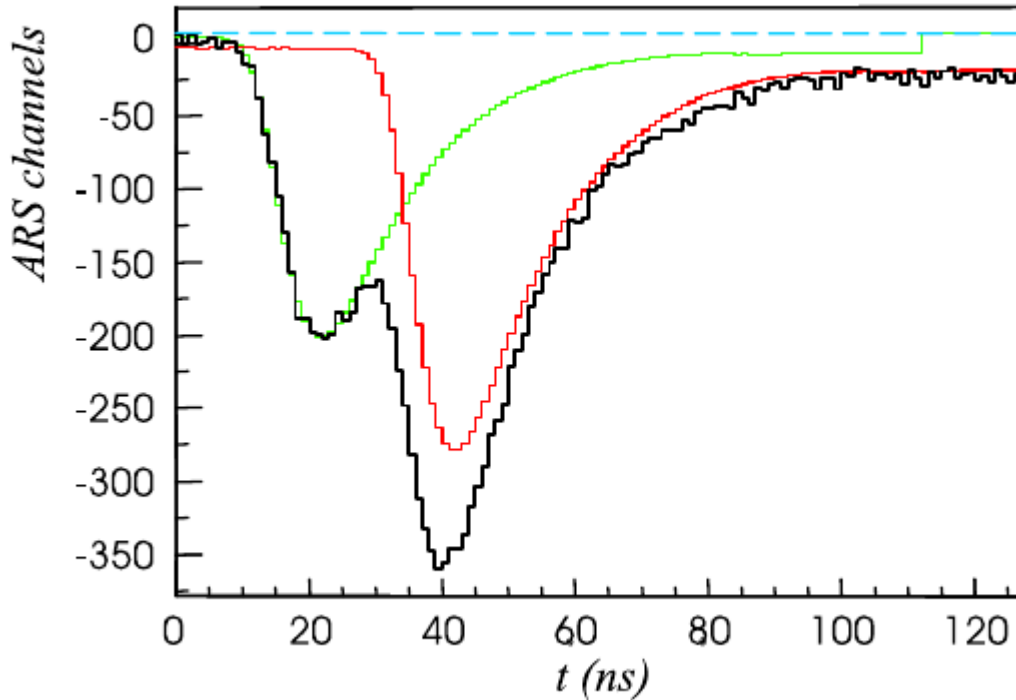

Figure 14: An example of ARS signals recorded in a 128 ns window. The ARS take a snapshot of the signals every nano-second and provide a good time and energy resolution for subtracting pile-up events like the ones shown in this figure. This figure was taken from [1].

The calorimeter has a dedicated trigger module that assesses the presence of a photon. Since the experiment will be conducted in hall A, high luminosity (10^{37} s^{-1} cm^{-2}) and kinematic settings which will require the calorimeter to be at small angles and close to the target imply very event high rates, approximated to be about 10 MHz for some kinematics [1]. Such high rates are associated with large pile-up events (like the ones shown in figure 14) which would make the ordinary ADCs not reliable in terms of time and energy resolution. For better rejection of pile-up events and better time and energy resolution, the Analog Ring Sampler chip was used. The ARS is a system of an array of 128 capacitor cells which continuously sample the signal at 1GHz [1]. Once sampling is completed, the signal is stored in capacitors and if they pass discrimination tests, it is digitized and ready to be sent as a valid photon signal to trigger data acquisition.

III.IV   Exclusivity of the DVCS reaction

The DVCS process is a three body final state channel. The photon will be detected by the DVCS calorimeter, the electron by the spectrometer, and the recoil proton will not be detected. Instead, exclusivity of the DVCS process will be ensured by the H(e,e'γ)X missing mass (M_X^2) technique. There are also other competing reactions that make the DVCS not easy to identify. The main competing channels are:

- π^0 production ($ep \rightarrow e'p'\pi^0$). The π^0 decays into two photons and is easier to identify if the decay is symmetrical and both photons are detected by the calorimeter. In an asymmetrical π^0 decay, one of the decay photons will be more energetic than the other [1] and will look more like a DVCS photon. The missing mass can not tell the difference between this and the DVCS process.

- associated DVCS (non-resonant)[1] ($ep \rightarrow e'N\gamma\pi$). An additional pion is produced and the lower its momentum is, the closer the missing mass of this reaction gets to the DVCS one.

- associated DVCS (resonant) [1] ($ep \rightarrow e'(\Delta \, or \, N^*)\gamma$). Here, the resonance decays into a pion and a nucleon. Since the first resonance is the $\Delta(1232)$, it means the minimum missing mass squared for this process is about 1.5 GeV^2.

The M_X^2 technique is based on using the information from the spectrometer and the calorimeter to compute the missing mass squared of the recoil proton as follows:

$$M_{ep->e'\gamma X}^2 = (k + p - k' - q)^2, \tag{28}$$

where k, p, k' and q are the 4-momentum vectors of the incident electron, the target proton, the scattered electron and the real photon, respectively. An example of the missing mass spectrum is shown in Fig. 15. To ensure exclusivity, a cut is then applied in the missing mass as shown in the figure. Since the proton does not break up in the process, M_X^2 should ideally be the mass of the proton (0.88 GeV^2). Instead, M_X^2 is dominated by the energy resolution of the calorimeter.

III.V   Data Acquisition

The data acquisition process will use the Cebaf Online Data Acquisition(CODA) system developed by the Jefferson Lab Data Acquisition Group[19]. The system consists of several data processing crates, each with a number of modules, all coordinated by CODA. Examples of hardware coordinated by CODA include VME digitization crates, front-end Fastbus crates, ethernet networks and a number of Unix computers. CODA supports all these and allows users to set experimental configurations such as choosing detectors that will form a trigger or triggers(in the case of multiple triggers) and the pre-sacle factors for each trigger. Finally, the trigger supervisor(TS) decides whether or not the DAQ should record an event.

The DVCS experiment will use the coincidence of a scattered electron and a photon to trigger data acquisition. The scattered electrons will be measured using the LHRS which will use a coincidence of the S2m and the gas Cherenkov sum to form an electron trigger. The Cherenkov will reduce the number of false triggers by negatively charged particles other than electrons.

The DVCS trigger module is a level 2[2] type of trigger. As mentioned earlier, the DVCS calorimeter

---

[2]A trigger is a system that uses a programmed criteria to decide (select) which events in a detector should be recorded. Triggers are usually designed in levels. A level 1 trigger selects data that becomes an input to a level 2 trigger. In this experiment, the HRS trigger is the level 1 and the DVCS trigger acts secondary to it.
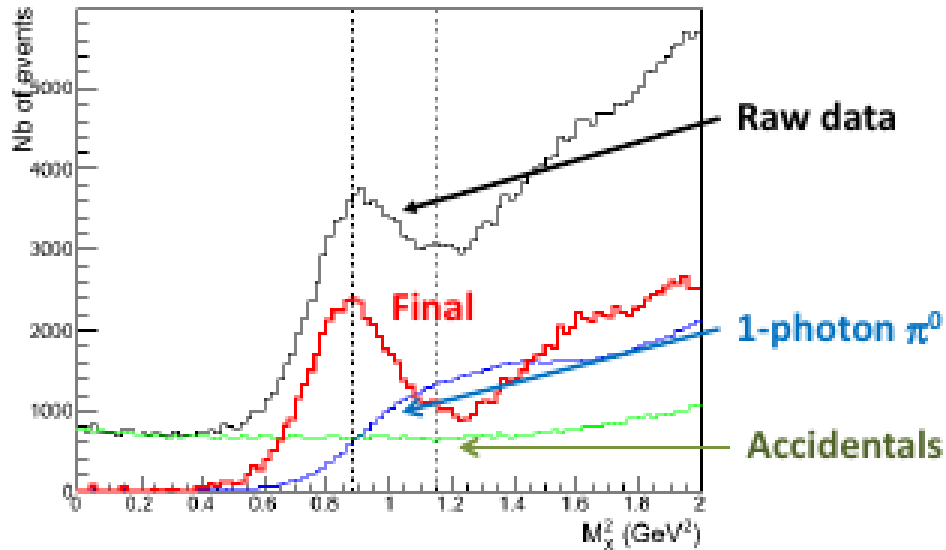
Figure 15: $ep \to epX$ missing mass squared. The peak (first from the left) is at the recoil proton mass squared and spread out because of energy resolution of calorimeter. The second peak is for background channels including π^0 events. This figure was taken from [14].

is close to the beamline and target which are main sources of noise. Therefore, a lot of time is invested in reading the ARS because proper selection of photons is important. To make the DVCS trigger, once the HRS has an electron event, all the ARS are stopped but not read [1]. An integration based on a 2×2 block "tower" of energy deposition is done for the calorimeter PMTs and then discriminated. An above threshold tower will indicate a DVCS photon in the calorimeter and the ARS are readout, leading to a final DVCS trigger sent to record the event.

IV   My Contribution to DVCS so far

The DVCS group is a collaboration with near-term and long-term goals. Two DVCS experiments have been done so far, in 2004 and 2010. Analysis of the 2004 and 2010 data is still in progress. In the near-term (fall of 2014), the third DVCS experiment is planned to start. This is the experiment that is the subject of this proposal. In future, another DVCS experiment has been approved to run in hall C of TJNAF. Prospects of doing DVCS on polarized ^{3}He in the future are also being studied. Up to this point, my contributions to the collaboration can be summarized as follows:

- Feasibility study for future DVCS experiments

    - When I joined the collaboration, I implemented a GEANT4 Monte-Carlo simulation to study the feasibility of DVCS on a polarized ^{3}He target using future facilities in hall C.

    - Starting from a DVCS calorimeter code developed by R. Paremuzyan and M. Defurme, I implemented the Hall C's High Momentum Spectrometer and a new 40 cm ^{3}He target cell and target chamber. I also coded Fermi motion effects and an interface between the simulation and the VGG model of GPDs to compute the cross section for each simulated event.

– Computation went beyond previous work performed with central kinematics only [24]. No significant effect was observed with the latest computation. Inclusion of Fermi momentum also did not have a big effect in the computation. Results from this work were documented and a report was submitted and presented to the collaboration. I presented a poster at the TJNAF annual user group meeting in June 2014, receiving honorable mention. The poster was also presented at the National Nuclear Physics Summer School in Williamsburg, July 2014.

- Preparation of the E12-06-144 Experiment

    – Since I came on-site to TJNAF, I have been part of a team involved in projects related to the upcoming DVCS measurement in Hall A. This entailed maintaining and optimizing the performance of the spectrometer's detectors, in particular the VDC and the straw chambers and the cosmic calibration of the DVCS calorimeter as assembled in Hall A.

        * In-depth analysis of HRS and calorimeter using cosmics.

    – I also participated in the 12 GeV commissioning of Hall A between March and April, 2014. Using the data taken during commissioning runs, I managed to do analysis to check the performance of the spectrometer detectors with beam.

        * The efficiency of the S2m and the gas Cherenkov was found to be better than 99% with 2-10 μA CW beam. Both detectors were also found to have a very good geometrical efficiency. A 1% inefficiency (relative to other PMTs) was observed in the left PMT of paddle thirteen of the S2m. This PMT is suspected to have a lower gain and its high voltage was recently adjusted. There has not been a good run to test the effect of the high voltage adjustment, which can be quickly done with beam or a very long cosmic run.

IV.I   GEANT4 Simulation of Polarized DVCS Observables Off ^{3}He Target(Future DVCS Experiments)

As briefly highlighted in section (II), the GPD E, in the forward limit, is an important missing information to Ji's sum rule. This GPD is suppressed in proton experiments but expected to dominate in the neutron system. This makes the neutron an interesting candidate for future experiments. However, free neutrons do not last long enough to make them useful in these experiments. In the absence of free neutrons, the spin structure attribute of polarized ^{3}He provides an effective free neutron when polarized. Theoretical studies by Refs. [20] have shown that at low momentum transfer to the ^{3}He nucleus, the sum of the GPDs E and H is dominated by the neutron contribution. To explore the possibility of extracting DVCS observables on this system, the experiment was implemented in a simulation.

In the simulation, DVCS events are generated uniformly in Q^2, x_B,t, ϕ and ϕ_e, (see section III). ϕ_e is the azimuthal angle of the scattered electron around the beamline direction. An event generator generates a vertex along the beam axis. The vertex is uniformly distributed along the target length. External pre-vertex radiative corrections are applied to the incident electron up to the vertex point. At the vertex, a scattered electron is then generated in the x-z plane such that the electron is scattered towards the HMS. The scattered electron is generated in a range in Q^2, x_B and ϕ_e,with the requirement that it falls within the angular and energy acceptances of the HMS. Internal post vertex radiative corrections are applied to the scattered electron.

The DVCS event generation is completed by the generation of t and ϕ, randomly. t is chosen in a range $[t_{min}, t_{max}]$ and ϕ in the range [0,2 π]. The last step is to check if the electron hits the HMS and the photon hits the calorimeter. If that's the case, an electron and a photon are assigned as primary

particles. For each DVCS event, the DVCS cross section is calculated based on the VGG model of GPDs by Vanderhaegen, Guichon and Guidal [23]. The VGG code computes cross sections for three target polarizations: Transverse x, Transverse y and Longitudinal directions. The target polarization direction is defined with reference to the direction of the beam, the longitudinal being in the beam direction, usually denoted as the z direction. The Tranverse x is defined in the plane of the beam line(horizontal plane), perpendicular to the z direction, forming the x-z plane with the beam direction. The transverse y is in the plane perpendicular to the x-z plane. These events and all their parameters are later saved into a ROOT file for post simulation analysis to estimate "experimental" rates and the corresponding statistical uncertainty.

Each qualifying DVCS event has five corresponding doubly polarized cross sections; $d^4\sigma^{++}$, $d^4\sigma^{+-}$, $d^4\sigma^{-+}$, $d^4\sigma^{--}$ and $d^4\sigma^{total}$. The superscripts correspond to beam(first) and target(second) polarization direction. The beam is always polarized along the direction of the virtual photon($\pm z$). The target can be polarized along $\pm x$, $\pm y$ and $\pm z$. $d^4\sigma^{total}$ is the un-polarized cross section. From these cross sections, many DVCS observables can be calculated. In this work, the Target Spin (TS) and Double Spin (DS) cross sections were computed;

$$\sigma^{DS} = \sigma^{++} - \sigma^{+-} - \sigma^{-+} + \sigma^{--} \tag{29}$$

$$\sigma^{TS} = \sigma^{++} - \sigma^{+-} + \sigma^{-+} - \sigma^{--}. \tag{30}$$

The kinematics settings used in the simulation are shown in Table 1 and the results in figures 16, 17 and 18.

Table 1: Central kinematics and other Parameters used in the simulation

k = incident beam energy	8.8 GeV
P_{HMS} = HMS central momentum	4.29 GeV
θ_{HMS} = HMS central angle	16.32 deg
θ_{calo} = Calorimeter central angle	-14.57 deg
d_{calo} = Calorimeter distance	157.6 cm
x_B	0.36
Q^2	3.05 GeV^2
P_t = target polarization	0.7
P_b = beam polarization	0.8
L = Neutron Luminosity	10^{37} $cm^{-2}s^{-1}$
^3He density	0.165 $kg\ m^{-3}$
Target length	40 cm
T = Experiment Duration	168 hours per helicity state

IV.II Preparation of the E12-06-144 Experiment

One of my longer term goals is to do a normalization study through Deep Inelastic Scattering (DIS) cross section extraction for the upcoming experiment, E12-06-114. The DIS cross section has been measured for over five decades and is well known over a wide range of kinematics. Since part of the DVCS trigger will be an electron trigger (S2m and gas Cherenkov coincidence), the cross section of the inelastic scattering of electrons on a proton target can be extracted. The DIS cross section extraction
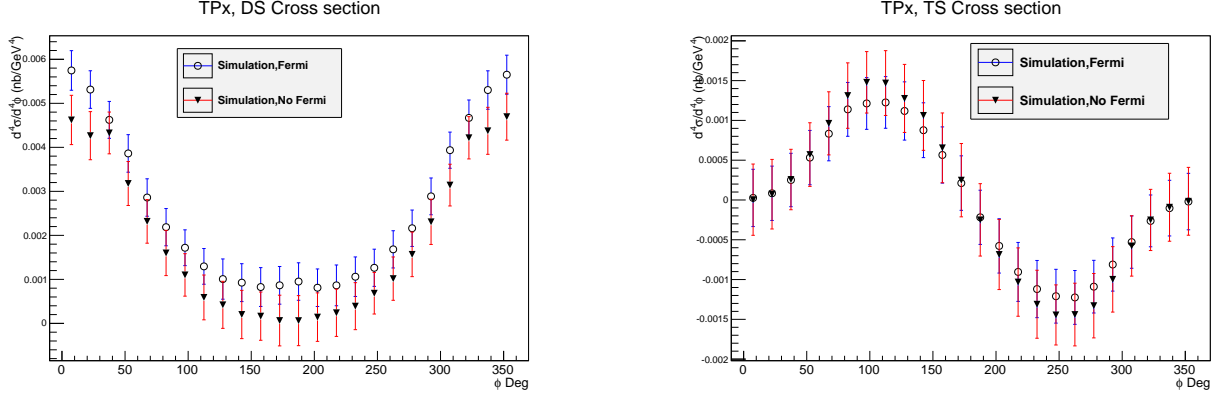
Figure 16: Simulation results of the cross section of the DVCS process on the neutron with(blue) and without(red) Fermi smeared kinematics for a Transverse x polarized target, based on the VGG model. On the left is the DS observable, and the TS observable on the right.
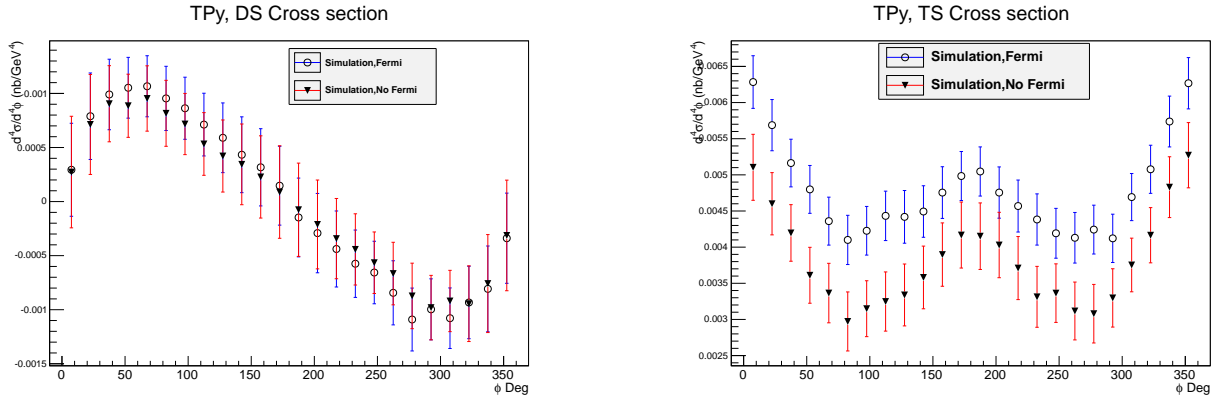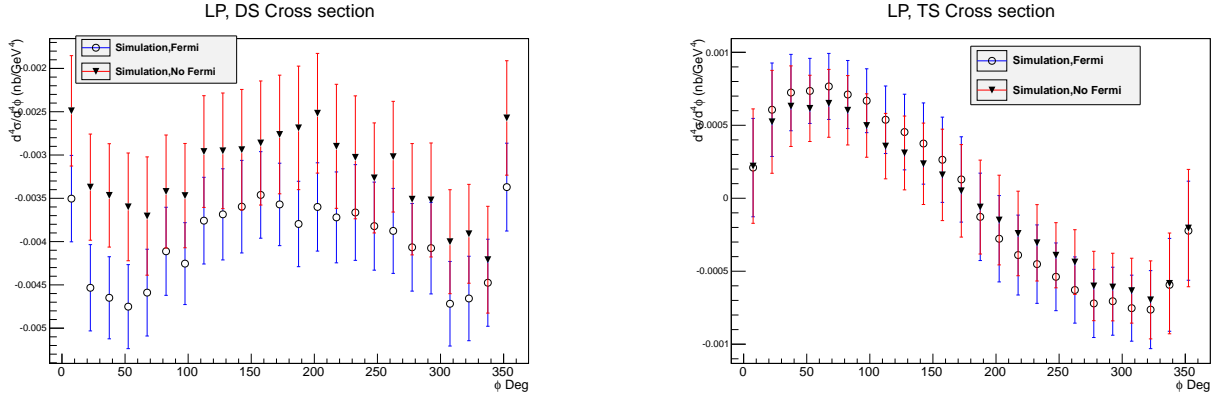

Figure 17: Simulation results of the cross section of the DVCS process on the neutron with(blue) and without(red) Fermi smearing for a Tranverse y polarized target. On the left is the DS observable, and the TS($-t < 0.4 \ GeV^2$) observable on the right.

Figure 18: Simulation results of the cross section of the DVCS process on the neutron with(blue) and without(red) Fermi smeared kinematics for a Longitudinally polarized target. On the right is the TS observable ($-t < 0.4 \ GeV^2$) and the DS observable is shown on the right.

will be essential in checking the quality of our data and normalization of the DVCS cross section. To extract the DIS cross section, very good knowledge of the following quantities is required:

- Number of electrons detected in the spectrometer

- Total number of electrons incident onto the target

- Length of the target

- Density of the target

- Efficiency (ϵ) of the DIS trigger. For a coincidence, this quantity is the product of the detectors forming the coincidence ($\epsilon = \epsilon_1 \times \epsilon_2$)

- Acceptance of the spectrometer

At the moment, my goal has been to focus on analysis and optimization of detector performances in preparation for production. This involved using sources of ionizing particles such as cosmics to investigate and fix inefficient detectors or detector components.

IV.II.1   HRS Detector Package Performance

Since coming to TJNAF, I have had the opportunity to participate and contribute to many luminosity related projects in the Hall A. I recently had the chance to be part of the 12 GeV commissioning process, resulting in taking data with beam in March-April of 2014. It is data from these runs that has been useful in checking different detector performances(with beam) before the productions runs. The commissioning data made it possible to study the efficiency of the S2m and Gas Cherenkov detectors and were found to be above 99% on average. The efficiency for S2m is shown in figure 19.

I also have the opportunity to work with hardware maintenance and optimization of the spectrometers. The DVCS experiment will be running in parallel with the GMP experiment(Precision Measurement of the Proton Elastic Cross Section at High Q^2, E12-07-108). This group has been responsible for the Hall A facilities for the past nine months or more and I have been able to join and work with them. With this group, I was given the responsibility to maintain and optimize the performance of the Vertical Drift Chambers(VDC) and the Straw Chambers, together with another GMP student colleague.

The VDCs use an argone-ethane environment and a set of four wire planes, U1, U2, V1 and V2 to construct coordinates and angle of a charged particle in the detector coordinate system. As a charged particle crosses the VDCs, it ionizes the gas producing ions and electrons. A strong electric field forces this charge to drift towards and get collected by the wires. Electronics readout cards collect this voltage signal for pre-amplification, discrimination, and then sends it to start the TDCs. A common stop is provided by the event trigger [25]. The straw chambers use a similar principle of operation but instead have their wires in straws filled with the gas environment. Many problems can arise during operation, from the individual wires to readout cards, power supplies, TDC electronics modules, up to software. As an example, during one performance test with cosmics, a couple of readout cards for the straw chambers(each card has 2 channels, each channel reading out 8 wires) were found dead(meaning a consecutive set of 16 wires were missing) and one card having one dead channel(8 wires missing). It was concluded that the problem as a non-stable power supply to the chambers and resulting in a couple of dead fuses from time to time. This process of optimizing the detectors will go on until the hall is closed for production. A sample of results from such exercises is shown in figure 20.

The VDCs are fully functional and recent cosmic tests have shown an above 95% efficiency on the left arm, for all wire planes. On the right arm, all planes have, on average, an above 95% efficiency
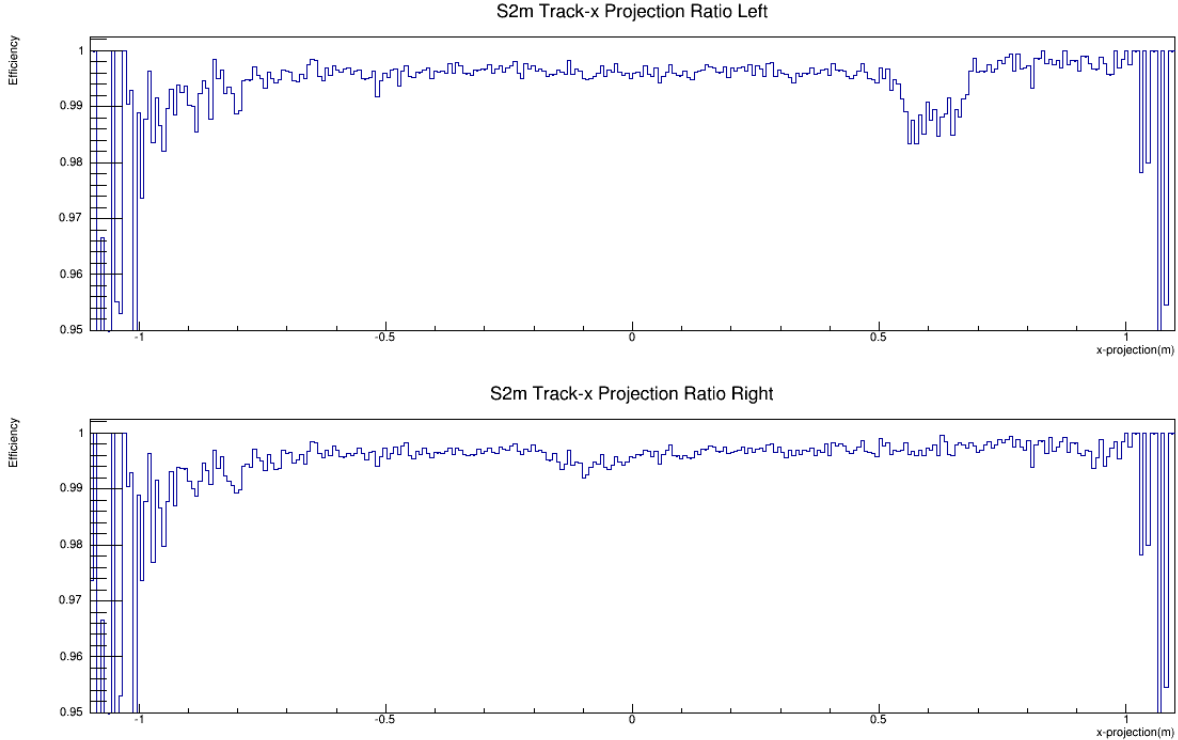
Figure 19: Results of the S2m efficiency studied using commissioning data. The efficiency was studied for both the right and the left PMTs of the S2m and found to be above 99% on average. A 1% inefficiency (relative to other PMTs) was observed in the left PMT of paddle thirteen. This PMT is suspected to have a lower gain and its high voltage was recently adjusted. There has not been a good run to test the effect of the high voltage adjustment. This can be quickly checked with beam or a very long cosmic run.

except for the U2 plane which has a lower efficiency. A number of tests were conducted to diagnose the problem, such as low and threshold voltage stability checks and using radioactive (^{55}Fe) sources to test the individual wires for analog signals and they were found to be operational. Further diagnosis concluded that the problem was with the readout cards and better performing cards will need to be installed. This was confirmed by swapping readout cards which had very good efficiency with those which were performing poorly. Results before and after a swap between two cards is shown in figure 21.

IV.III   DVCS Calorimeter Calibration Using Cosmics

Calibrating the calorimeter entailed adjusting the high voltage (HV) of the PMT of each of the 208 channels or blocks of the calorimeter such that for the same energy deposition, we get the same signal size. In this case, the calibrated signal was the integral of the ARS for each channel. The goal was to align the integrated ARS signal such that for each channel, the gain is 3000 channels above pedestal (chosen to be clearly above pedestal).

The energy deposition of ionizing particles depends on the length of the material traversed by the particle. Therefore, to ensure a selection of events with a uniform energy deposition, a cut was applied to select cosmics that have made approximately the same path lengths across all calorimeter blocks. This was done by selecting vertical cosmics only. The vertical cut was applied offline by demand-

ing a large integrated ARS signal both at the top and bottom of each column. After the vertical cuts, the cosmic spectrum for each channel was fitted by a Gaussian. The HV for each channel was then calculated in such a way that it moves the mean of the fit to the goal of 3000 channels. This can be interpreted as the value assigned to represent the signal size for cosmics (energy about 30 MeV).

To adjust the HV, we consider the relative gain, defined as:

$$G = \alpha HV^{\beta}, \tag{31}$$

where β is a block specific parameter which is on average, approximately 7. For each iteration (calibration step), the next HV values were calculated as:

$$HV_2 = HV_1 \left(\frac{G_2}{G_1} \right)^{\frac{1}{\beta}}, \tag{32}$$

where G_1 and HV_1 are the starting gain and HV respectively. G_2 and HV_2 correspond to the target gain (3000) and the HV set to achieve this target.

Results and Conclusions[3]

At the last iteration, the mean achieved gain was 3053 channels for the ARS and about 266 channels for the ADC. Both the ARS and the ADC were cross-calibrated to about 4.5% and 5.3%, respectively, see Figs. 22. Two channels, 140 and 170 were found to have a relatively low gain and they were already set to maximum HV. During production, these channels will have their HV increased relative to the rest.
Further analysis was done to study the correlation of the energy(ARS)and the trigger (ADC) across all channels. A uniform correlation across all channels would mean a uniform threshold can be applied for the calorimeter[27]. Correlation plots were fitted with a linear function and the slope was deduced, see Fig. 22. On average, the correlation is uniform, except for two channels, 90 and 127. These two have a lower correlation slope and are still under investigation.
Noise studies were also done by looking at the ratio of the standard deviation for the selected cosmic spectrum for each channel to the mean of the Gaussian fit. A high ratio is an indication of a noisy PMT/channel. A few channels, 2, 18, 23, 31 and 192 were found to be relatively noisy, see Fig. 24.
Lastly, arrival times for cosmics across all channels were studied and were found to be uniform. This is important because the trigger gate window (start and width) is uniform. Signals arriving much earlier or later will miss the gate and information about them will be lost or partially recorded. Arrival times are shown in Figs. 25.

---

[3]This project is in parallel with other DAQ projects. Some parameters, like trigger timing, will change from time to time, depending on modifications done to the data acquisition software and hardware.
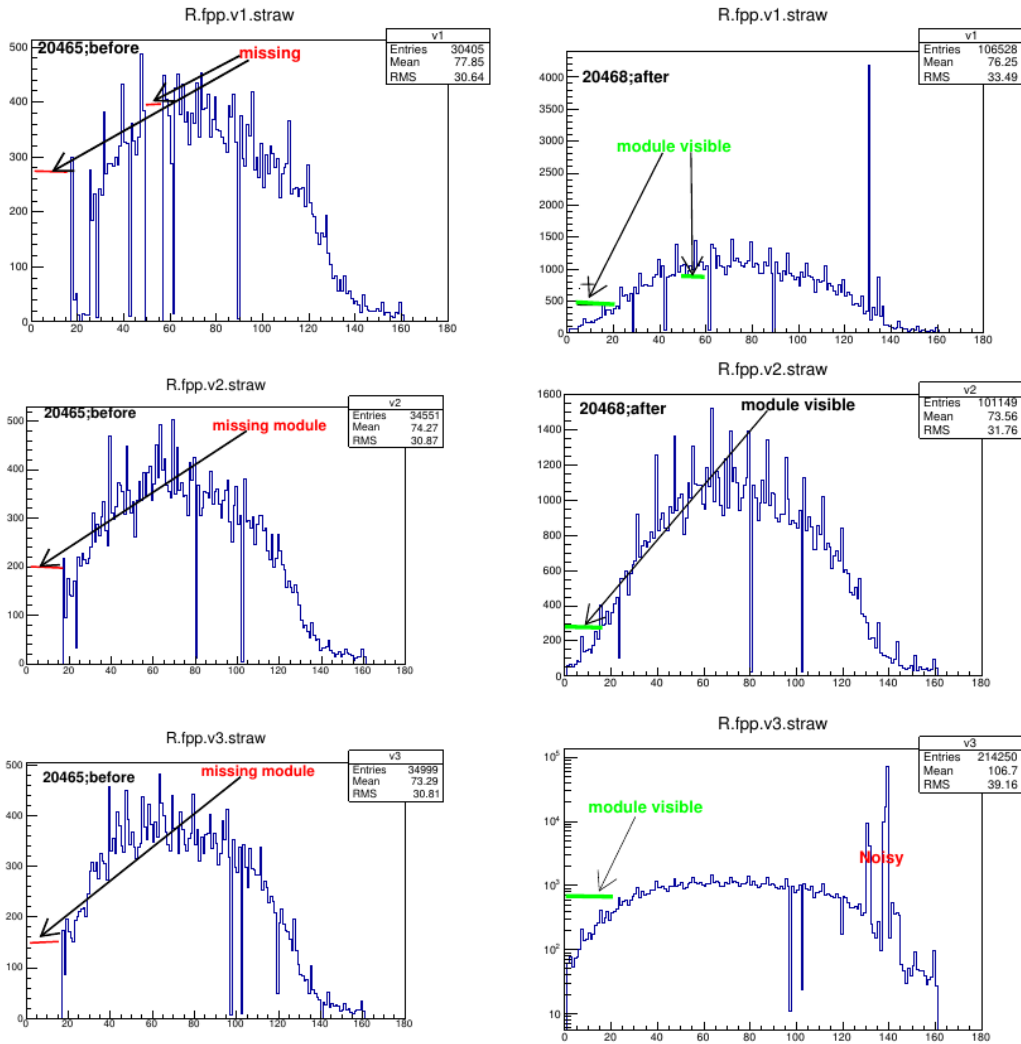
Figure 20: Some results obtained using cosmic tests before and after working on the straw chambers on the RHRS. An unstable power supply resulted in a number of dead readout modules and was removed.
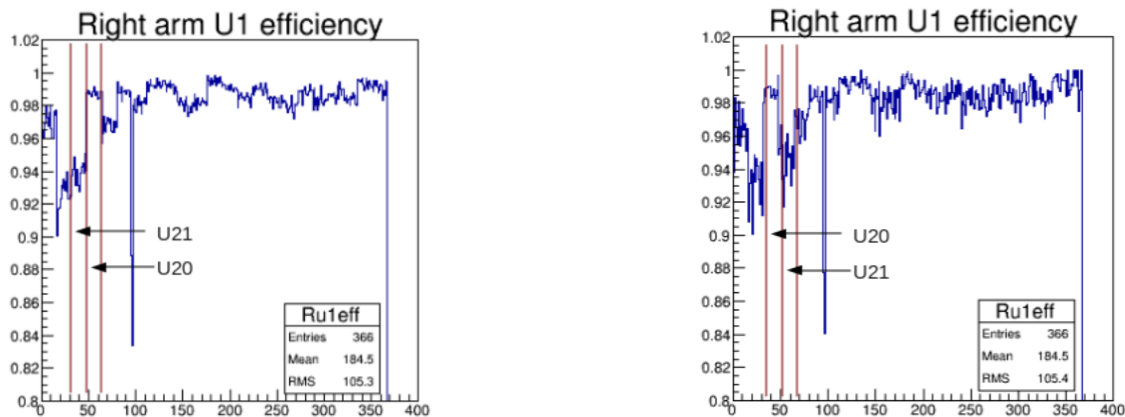

Figure 21: Results of VDC wire efficiency for one plane of wires, before swapping readout cards(left) and after(right). The readout card number 21 is seen to move with the inefficiency, indicating a problem with the readout card itself, instead of other electronic components of the system.
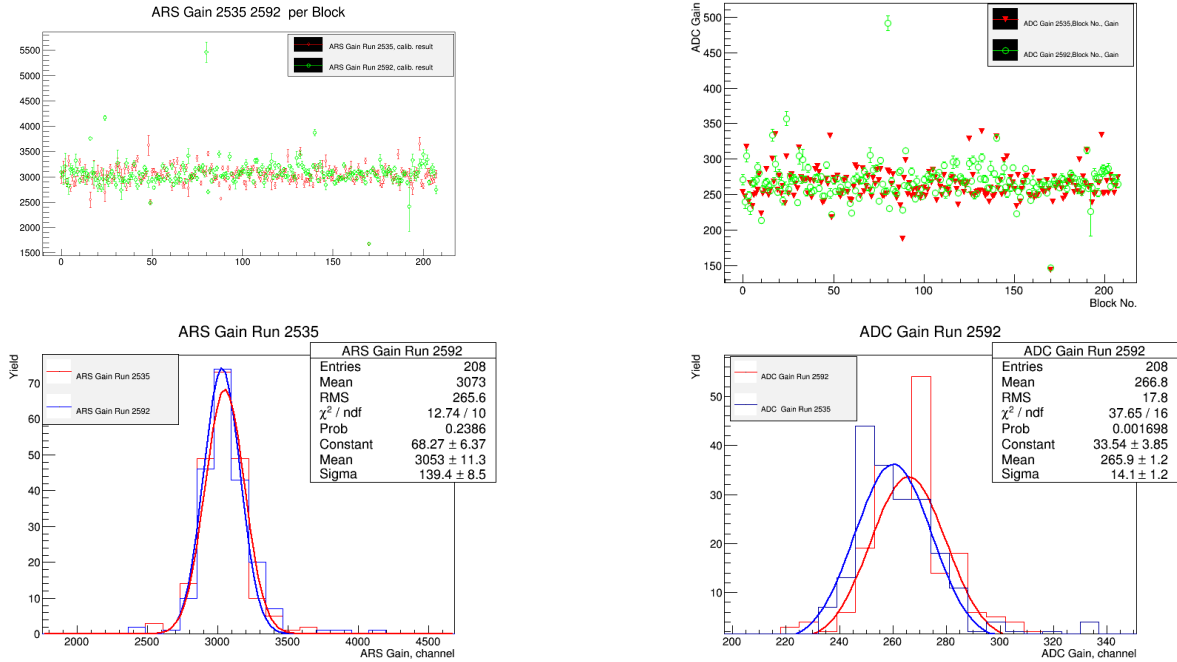
Figure 22: Results of the last calibration iteration. Left column: results of the calibration of the integrated ARS signal for each of the 208 channels corresponding to the 208 blocks/PMTs of the calorimeter. Right column: calibration results of the ADC signals as a function of channel. Top panel: the mean gain as obtained from the fit of the selected cosmic spectrum in each channel. Bottom panel: histograms of the means, fitted with a Gausian. The results of the last two calibration steps are shown in each case, for comparison.
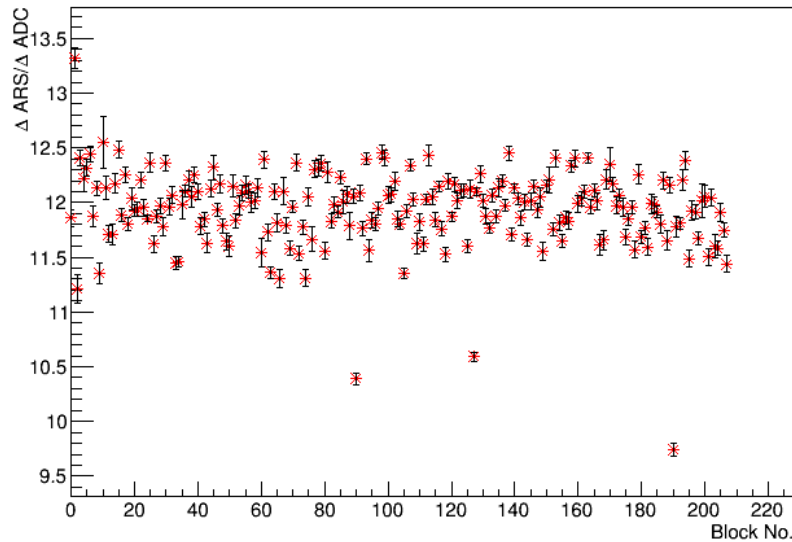

Figure 23: Slopes of the ARS:ADC correlation as a function of channel number from the last calibration run(2592). On average the slope is about 12-13. Channels 90, 127 and 190 were found to have lower than average slopes. After investigations, ARS 190 was found to be a bad channel and has since been replaced.
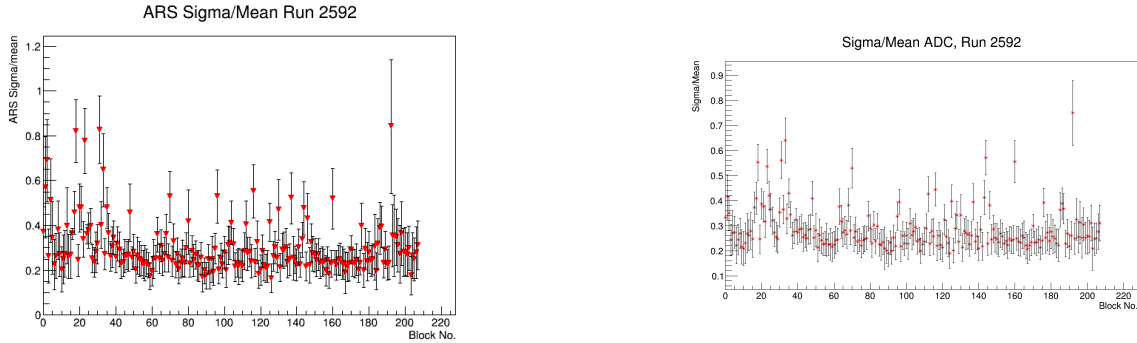
Figure 24: The ratio of the sigmas to the mean gain as a function of block number for the ARS (left) and ADC (right) signals. Relatively noisy channels: 192, 18, 31, 23, 2, and 33. All of these, except for 18, 23 and 33 are at the edges of the calorimeter (the edges are cut out during offline analysis). These can be moved to the edges too, in the future.
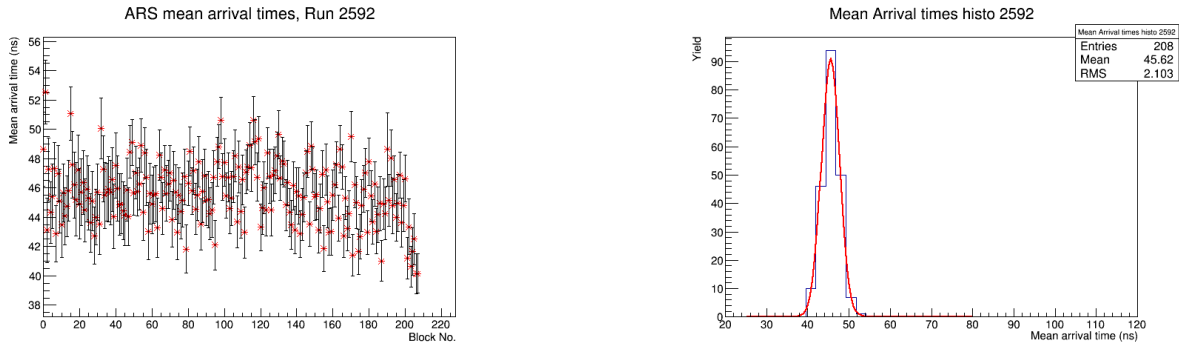

Figure 25: Arrival times for ARS signals. Left panel shows the average arrival time for each channel. The left panel shows a histogram of the means shown on the left, fitted with a Gaussian. A mean arrival time: $T_{arrival} = 45.60 \pm 2.2$ ns is obtained from the fit.

V Thesis Goals and Time-line

Goals

My proposed thesis work is aligned with achieving the goals of the DVCS collaboration, in particular, for the E12-06-144 experiment. The main goals and the physical insights they will reveal are summarized in section III.

Time-line

Since joining the department as a graduate student in 2011, I have completed six out of seven mandatory classes. I spent one year working in Dr. Castillo's group before joining DVCS. Currently, I'm in Newport News(at TJNAF) in preparation for the upcoming DVCS production running. I plan to move back to Athens in the Fall of 2015 to the end of my studies. During that period, I plan to take the remaining class(graduate lab) and a couple of other classes that will be of interest to my research. Table 2 shows a historical and proposed time-line since joining the department to putting together my thesis, culminating in a Spring 2017 (six years after starting) graduation.

Table 2: Time-line of work

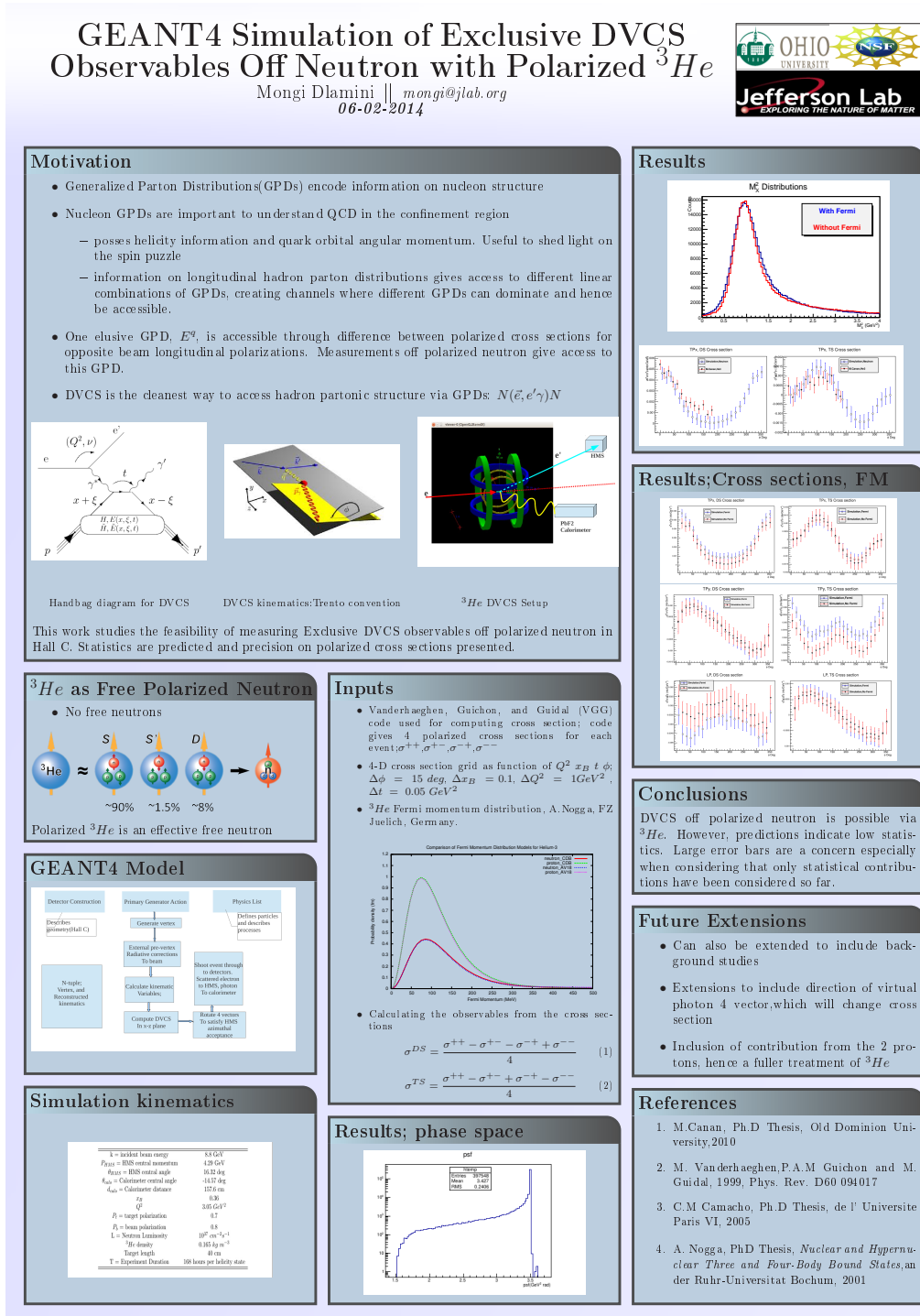| Activity	F 11	Sp 12	Su 12	F 12	Sp 13	Su 13	F 13	Sp 14	Su 14	F 14	Sp 15	Su 15	F 15	Sp 16	Su 16	F 16	Sp 17
Classes	■	■		■	■		■										
Castillo		■	■			■	■										
Joined DVCS							■										
Move to TJNAF								■									
Experiment prep.								■	■								
Production										■	■	■					
Move to Athens													■				
Remaining classes														■	■	■	
Data Analysis													■	■	■	■	■
Thesis writing																■	■
Thesis Defence																	■

A   APPENDIX: GEANT4 Simulation Poster

Figure 26: Poster on GEANT4 simulation presented at the joint Halls A and C meeting in June 2014 and at the NNPSS in July 2014.

References

[1] C. Muñoz Camacho, PhD Thesis, de l'Universite Paris VI,2005

[2] J. Dudek et al. , Eur. Phys. J.A(2012) 48:187

[3] United States Department of Energy,National Science Advisory Committee, Long Range Plan 2007. Retrieved from;http://science.energy.gov/np/nsac/

[4] Hyde, C. E., Radyushkin, A., and Guidal, M. (2011). Deeply Virtual Exclusive Processes and Generalized Parton Distributions.. J.Phys.Conf.Ser., 299, (pp. 012006-012029).

[5] B. Guegan, PhD Thesis, Universite Paris-Sud, Rensselaer Polytechnic Institute,2013

[6] A. V. Belitsky and A. V. Radyushkin, Phys. Rept. **418**, 1 (2005) [hep-ph/0504030].

[7] M. Guidal, H. Moutarde and M. Vanderhaeghen, Rept. Prog. Phys. **76**, 066202 (2013) [arXiv:1303.6600 [hep-ph]].

[8] M. Diehl, arXiv:hep-ph/0205208v2, 9 Sep. 2003

[9] M. Mazouz et al.,Phys.Rev.Lett.99:242501,2007

[10] X.D. Ji, Phys.Rev.Lett. 78 (1997) 610-613

[11] C. Muñoz Camacho, Habilitation Thesis, de l'Universite Paris VI,2014

[12] A. Radyushkin, Phys.Rev. D59,014030(1999)

[13] D. Mueller et al., Fortschr. Phys. 42,101(1994)

[14] A. Camsonne,C. Hyde, C. Muñoz Camacho and J. Roche, et al., E12-06-114 Proposal Update to PAC, Retrieved from: http://www.jlab.org/exp_prog/proposals/06/PR12-06-114_update.pdf

[15] J. Roche, C. Hyde, B. Michel, C. Muñoz Camacho et al., E12-06-114 Proposal, Retrieved from: http://www.jlab.org/exp_prog/proposals/06/PR12-06-114.pdf

[16] A.V. Belistky, D. Muller and A. Kirchner, Nucl.Phys. B629 (2002) 323-392

[17] A. Biselli et al.,E12-06-119, Retrieved from: http://www.jlab.org/exp_prog/proposals/06/PR12-06-119.pdf

[18] J. Roche et al., E12-06-114, Retrieved from: http://www.jlab.org/exp_prog/proposals/06/PR12-06-114.pdf

[19] J. Alcorn, *et al.*, Nucl. Instrum. Meth. A **522**, 294 (2004).

[20] M.Rinaldi, S.Scopetta, arXiv:1208.283v1[nucl-th],14 March 2013

[21] *https : //phys.cst.temple.edu/ meziani/Temple_University_3He_Lab_files/helmholtz.htm*

[22] *http : //pol3he_daq.physics.wm.edu/ pol3he/Setup/RFCoils.php.*

[23] Vanderhaeghen M, Guichon P A M and Guidal M, 1999 Phys. Rev. D60 094017

[24] M. Canan, PhD Thesis,*Triple Coincidence Beam Spin Asymmetry Measurement in Deeply Virtual Compton Scattering*, Old Dominion University.

[25] K. G. Fissum, W. Bertozzi, J. P. Chen, D. Dale, H. C. Fenker, J. Gao, A. Gavalya and S. Gilad *et al.*, Nucl. Instrum. Meth. A **474**, 108 (2001).

[26] A. Nogga, PhD Thesis, an der Ruhr-Universitat Bochum, 2001

[27] C. Muñoz Camacho, Private communication

[28] M. Dlamini, Technical report. Found at: https://hallaweb.jlab.org/dvcslog/DVCS12GeV/1